Induced polarization of volcanic rocks. 3. Imaging clay cap properties in geothermal fields

A. Revil, Y Qi, A. Ghorbani, A. Coperey, A. Soueid Ahmed, Anthony
Finizola, T Ricci

Induced polarization of volcanic rocks. 3. Imaging clay cap properties in geothermal fields

A. Revil,[1] Y. Qi,[1] A. Ghorbani,[2] A. Coperey,[1] A. Soueid Ahmed,[1] A. Finizola[3] and T. Ricci[4]

[1]*Université Grenoble Alpes, Université Savoie Mont Blanc, CNRS, IRD, IFSTTAR, ISTerre, 38000 Grenoble, France. E-mail:* andre.revil@univ-smb.fr
[2]*Department of Mining and Metallurgical Engineering, Yazd University, Yazd, Iran*
[3]*Laboratoire GéoSciences Réunion, Université de la Réunion, Institut de Physique du Globe de Paris, Sorbonne Paris-Cité, CNRS UMR 7154, Saint-Denis, La Réunion, France*
[4]*Istituto Nazionale di Geofisica e Vulcanologia, Rome, Italy*

SUMMARY

Smectite-rich clay caps form permeability seals in geothermal systems. The presence of smectite is also responsible for a strong surface (interfacial) electrical conductivity and polarization due to their electrical double layer properties. We developed new complex conductivity models using both differential effective medium (DEM) and volume averaging theories accounting for both conduction and polarization of these high cation exchange capacity (CEC) materials. These models predict that the chargeability is also a non-linear function of the pore water conductivity reaching a constant value at pore water conductivity far above the so-called iso-conductivity point. The iso-conductivity point is characterized by the equality between the conductivity of the rock and the conductivity of the pore water. We apply the DEM conductivity model (which requires only two textural parameters) to smectite-rich volcanic and sedimentary rocks using data sets from the literature. When smectite is present in the volcanic rocks, the CEC of the rock is dominated by the CEC of smectite. The grain conductivity and the normalized chargeability are related to each other by a dimensionless number $R = 0.10$ (independent of temperature and saturation) and both are controlled by the excess of charge per unit pore volume Q_V, which can be determined from the CEC and porosity. Our petrophysical model is also able to predict the permeability of the rock as well from the CEC and the porosity. It is applied to a 3-D data set at Krafla volcano (Iceland). The porosity, the CEC, the percentage of smectite, and the permeability of the clay-cap are imaged by 3-D induced polarization tomography. Electrical conductivity tomography alone does not allow separation of the contribution of the bulk pore space from the interfacial properties related to alteration and therefore should be used with caution.

Key words: Electrical properties; Hydrogeophysics; Hydrothermal systems; Electrical resistivity tomography (ERT).

1 INTRODUCTION

Smectite and smectite-illite clays are generally found as alteration products in geothermal systems in the equilibrium temperature range from 50 to 200 °C (e.g. Browne 1978; Gunderson *et al.* 2000; Meunier 2005; Cumming 2009). Such smectite-rich clay caps form a key-component of geothermal systems because of their very low permeability, which can efficiently seal geothermal reservoirs and favour the presence of perched aquifers associated with water transfer through the vadose zone (Fig. 1). In turn, these seals can be detected by coupling the self-potential method with magnetotelluric data (e.g. Aizawa *et al.* 2009) or CO$_2$ soil gas concentration with electric resistivity tomography (e.g. Revil *et al.*

2011). In sedimentary basins, the smectite to illite transition starts at ∼50 °C and is expected to be complete at temperatures ranging from 80 to 140 °C (Colten-Bradley 1987; Freed and Peacor 1989). In geothermal systems, alteration of the volcanic glass implies the formation of smectite and mixed-layer illite-smectite clay minerals typically found at temperatures below ∼200–250 °C (Meunier 2005). The difference between the two types of systems is explained through the completeness of the water–rock interactions and the ability of ionic species to migrate (Jennings & Thompson 1986). Incomplete water–rock interactions reflecting low permeability away from the main groundwater flow paths often results in the presence of smectites and mixed-layer illite/smectite (I/S) clays in the rock matrix up to higher temperatures (Gunderson *et al.* 2000).
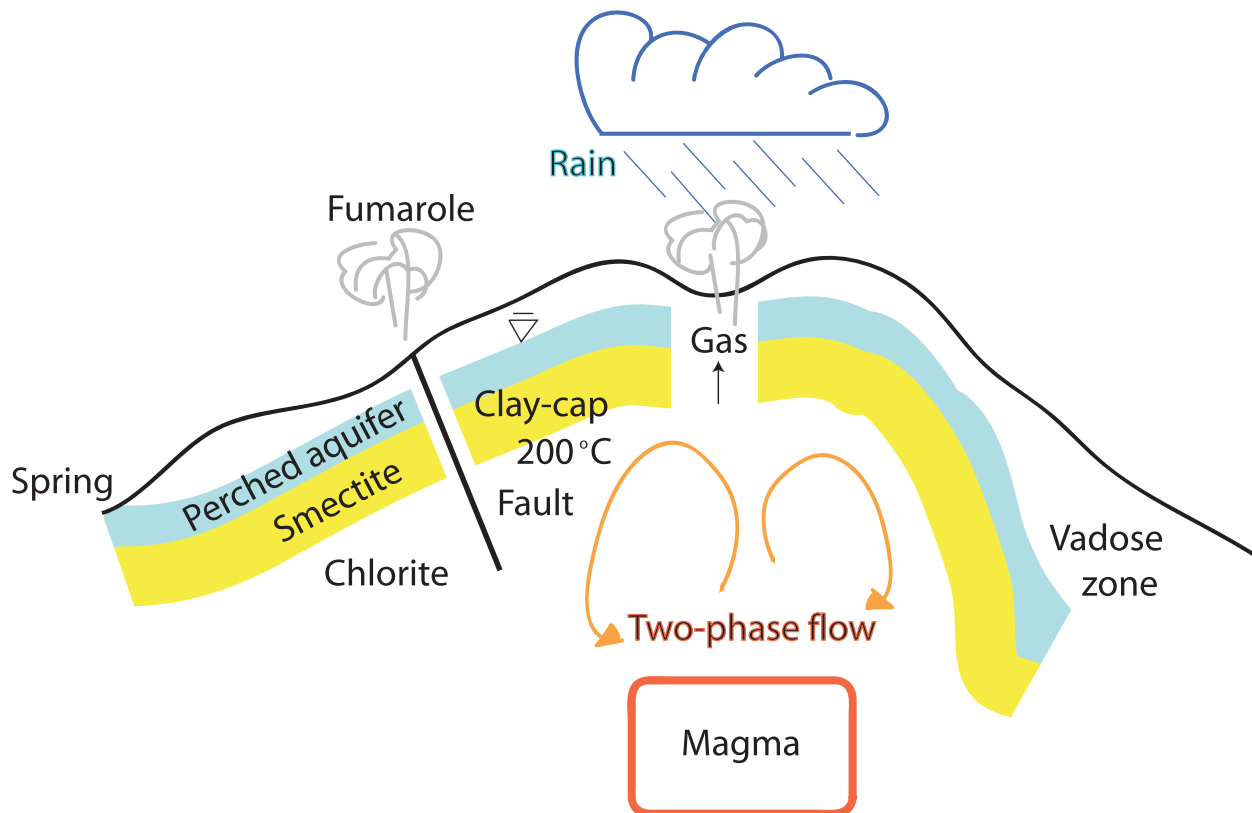
Figure 1. Sketch of a hydrothermal system with a clay cap rich in smectite. The bottom of the clay-cap corresponds usually to an isotherm of 200 °C (modified from Aizawa *et al.* 2009). Its low permeability favours the formation of perched aquifers and maintains two phase flow (steam and liquid water) below it. Our goal is to use induced polarization and conductivity imaging to identify such clay caps and to determine some of its properties including its porosity and permeability.

The association of smectites and I/S clays with temperature suggests that if smectite could be detected with geophysical methods, it provides a geothermometer (e.g. Cumming 2009; Cumming & Mackie 2009; Muñoz *et al.* 2010; Revil *et al.* 2018b). Because of the very high cation exchange capacity (CEC) of smectite and mixed layer illite-smectite clays (typically in the range 10–90 meq/100 g depending on the mass fraction of smectite), highly altered rocks are characterized by high electrical conductivity (>0.1 S m^{-1}, because of surface conduction) and polarization (Ghorbani *et al.* 2018). In geothermal systems, it is usually assumed that high conductivity values correlate with low permeability smectite-rich clay caps, lying over higher resistivity values (>100 Ohm m), higher temperature and permeable hydrothermal reservoirs (Cumming 2009). Electrical conductivity-based galvanometric and induction-based electromagnetic methods are routinely used to map the 1–0.1 S m^{-1} smectite clay alteration cap of geothermal systems (e.g. Bibby *et al.* 1995; Pellerin *et al.* 1996; Meju 2002; Cumming & Mackie 2009; Spichak & Manzella 2009; Muñoz 2014; He *et al.* 2016). However, caution should always be used in interpreting electrical conductivity data alone. Indeed, electrical conductivity cannot distinguish these clay caps from the presence of hypersaline fluids generally close to the magmatic chambers. Counter-examples exist. Revil *et al.* (2011) discussed indeed the presence of a clay cap at Stromboli volcano evidenced by the absence of soil diffuse degassing in the upper part of the edifice (Fossetta area). The permeability barrier (clay-cap) is located in a resistive body overlying a conductive hydrothermal system (Fig. 2). Great care should therefore be applied

in interpreting electrical conductivity imaging alone. In this paper, we show that induced polarization provides a complementary tool useable for the characterization of smectite and mixed layer illite–smectite clay caps in order to image some of their key properties such as the percentage of smectite, their porosity and their permeability.

A number of papers have already focused on describing the electrical conductivity of various types of smectites, such as montmorillonites, for a broad range of porosity from colloidal suspensions to consolidated materials (e.g. Sauer *et al.* 1955; Spiegler *et al.* 1956; van Olphen 1957; van Olphen & Waxman 1958; Fripiat *et al.* 1965; Cremers & Laudelout 1966; Gast 1966; Jorgensen & Low 1970; Shainberg & Levy 1975). A non-linear relationship between the conductivity of the material and the conductivity of the pore water is expected for high CEC materials at least at low pore water salinities. Such non-linear behaviours have been recognized in the literature for both synthetic cation exchangers (e.g. Revil 1999), smectite-rich soils (e.g. Shainberg *et al.* 1980), colloidal suspensions of smectite (e.g. Shainberg & Levy 1975; Lockhart 1980; Leroy *et al.* 2017) and shales (e.g. Wyllie & Southwick 1954; Vinegar & Waxman 1984). These experimental evidences have prompted the development of non-linear conductivity models (Sauer *et al.* 1955; Spiegler *et al.* 1956). A review regarding such non-linear behaviours of rocks with high cation exchange capacities can be found in Friedman (2005).

Induced polarization describes the ability of porous rocks to store reversibly electrical charges under the influence of a primary electrical field (e.g. Olhoeft 1985). In the two previous papers of this series
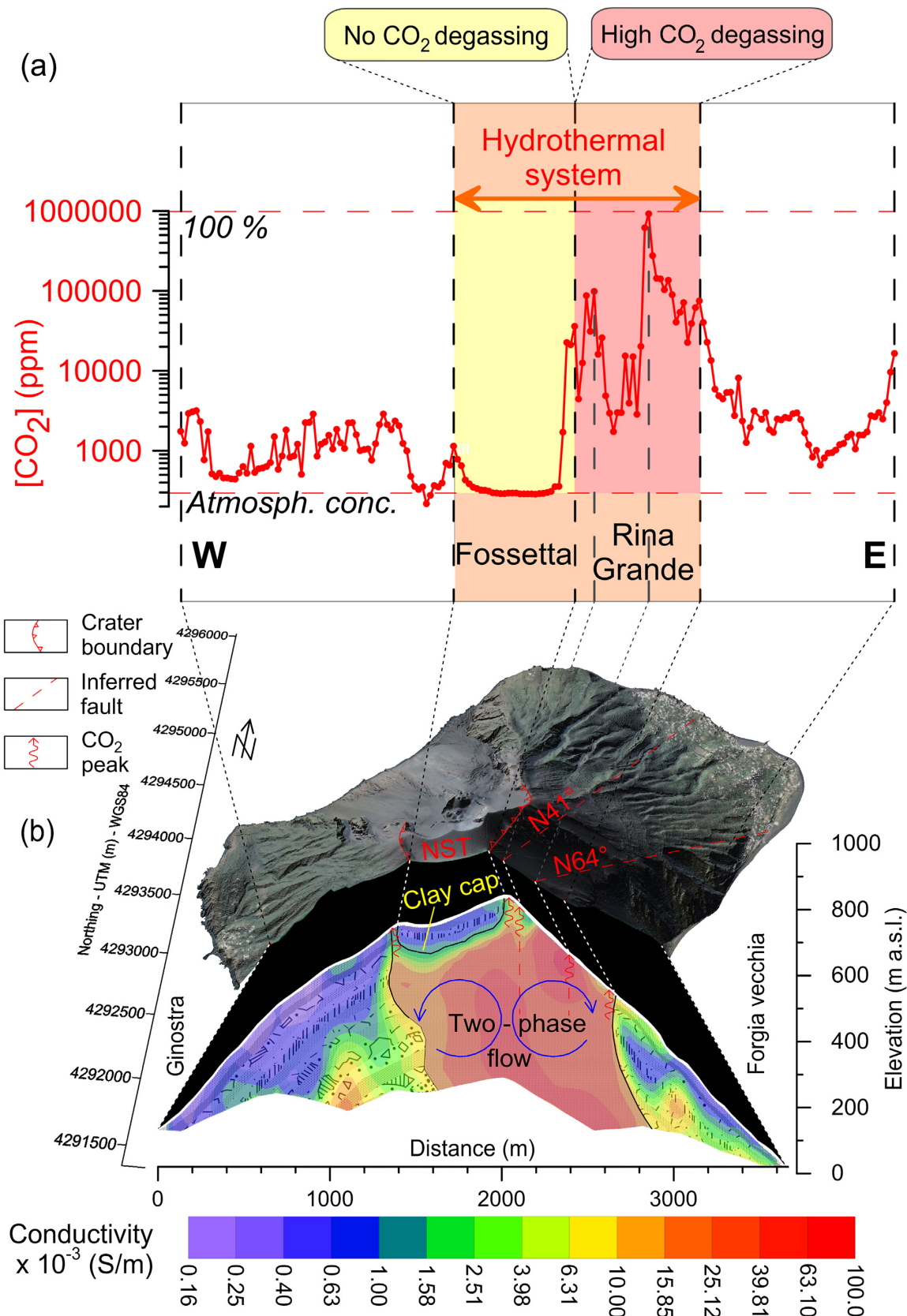
Figure 2. Example of clay cap evidenced at Stromboli using CO_2 soil degassing and dc conductivity imaging. (a) CO_2 soil concentration (in ppm). (b) Interpreted electrical conductivity tomogram of Stromboli. The conductive body corresponds to the hydrothermal system. 'NST' stands for NeoStromboli crater. N41 and N64 correspond to two major fault zones. Data are from Revil *et al.* (2011). The conductivity scale corresponds to the logarithm of the conductivity comprised between $\sim 10^{-1}$ and $\sim 10^{-4}$ S m^{-1}.
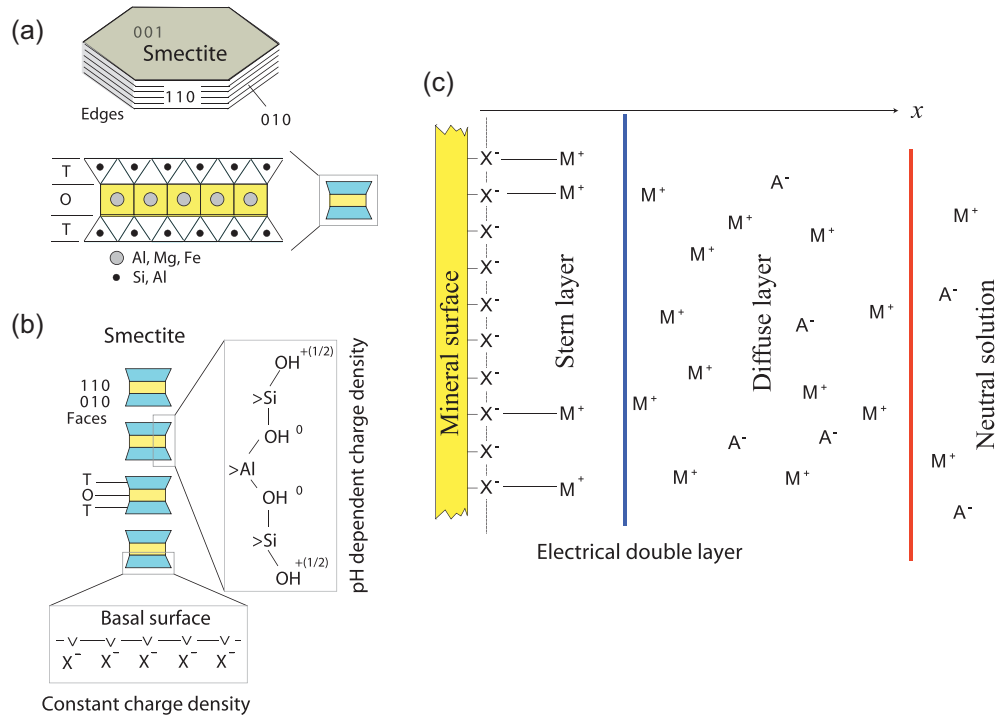
Figure 3. Smectite and electrical double layer. (a) TOT structure of the smectite particle (T: tetrahedral layer, Si; O: octahedral layer, Al). (b) The charge on the edge of the crystals (110 and 010 planes) is pH-dependent and due to both silanol and aluminol sites while the charge on the basal surface (001 plane) is due to the isomorphic substitutions in the crystalline framework. (c) The electrical double layer around the smectite comprises the diffuse and Stern layers, which screen the charge in the particle (due to isomorphic substitutions) and on its surface (amphoteric sites). M^+ denotes the metal cation (e.g. Na^+) while A^- denotes the anion (e.g. Cl^-). The groups X– denotes the negative sites on the mineral surface. This electrical double layer is central in defining both surface or grain conductivity and to understand the polarization of the grains and the porous material.

(Revil *et al.* 2017a,b), we have developed a comprehensive database of experimental data for induced polarization of volcanic rocks. In absence of metallic particles, one of the key properties used to describe induced polarization is the normalized chargeability, which is defined as the difference between the instantaneous conductivity of the rock and its direct current (dc) conductivity. As a side note, the term 'instantaneous' (in time-domain induced polarization) is synonymous with high frequency. In a similar way, the term dc (or steady state) is synonymous of low frequency in frequency-domain induced polarization. High and low frequencies are of course defined with respect to the main relaxation times describing the polarization process and typically associated with grain sizes. The normalized chargeability and the quadrature conductivity (a quantity proportional to the normalized chargeability) are proportional to the CEC (e.g. Vinegar & Waxman 1984). Therefore smectite-rich rocks are characterized by high normalized chargeability values because of their high CEC. In addition, a linear relationship has been observed between surface conductivity and normalized chargeability (Revil *et al.* 2017a,b).

Our goal here is to go further by providing a consistent model of electrical conductivity and normalized chargeability accounting for the effect of the water content and CEC and to connect the CEC to both the mass fraction of smectite and permeability. In Section 2, we develop the non-linear relationship between the complex conductivity of the rock and the pore water conductivity using the differential effective medium (DEM) theory. In Section 3, we revisit an alternative non-linear petrophysical model between the complex conductivity of the rock and the pore water conductivity based on the volume-averaging technique. The two approaches are extensively compared with experimental data and we present the

advantages and drawbacks of the two approaches. Then, we apply this model in Section 4 to a 3-D data set of induced polarization data recorded in the Summer 2017 at Krafla volcano, Iceland We show how the combination of the petrophysical model and the geophysical tomograms can be used to image the water content, the CEC, and the permeability. Krafla has already been broadly explored using geophysical methods and drilling operations (e.g. Mortensen *et al.* 2009). We believe that this model can be used to avoid a number of pitfalls in using electrical conductivity alone as already discussed in a number of papers (e.g. Bibby *et al.* 2005; Muñoz 2014).

2 DEM THEORY

Our first goal is to model the complex conductivity of rocks that are rich in smectite in order to apply induced polarization to map the clay cap usually found in geothermal systems (Fig. 1). The model should be however versatile enough to accommodate various alteration facies in hydrothermal systems including fresh (unaltered) volcanic rock samples. This work is a direct continuation of the works published in our two previous papers (Revil *et al.* 2017a,b), where we developed a model of induced polarization for volcanic rocks.

Smectite is a clay mineral characterized by very high CEC (typically around 90 meq/100 g). The CEC reflects the amounts of exchangeable surface sites (on all the crystalline planes including between the basal surface in the open interlayer porosity, Fig. 3). The charge on the mineral surface is compensated in the electrical double layer as well as by counterions populating the interlayer space of smectite (Fig. 3). The electrical double layer is composed by a Stern layer of sorbed counter-ions plus a diffuse layer in which the
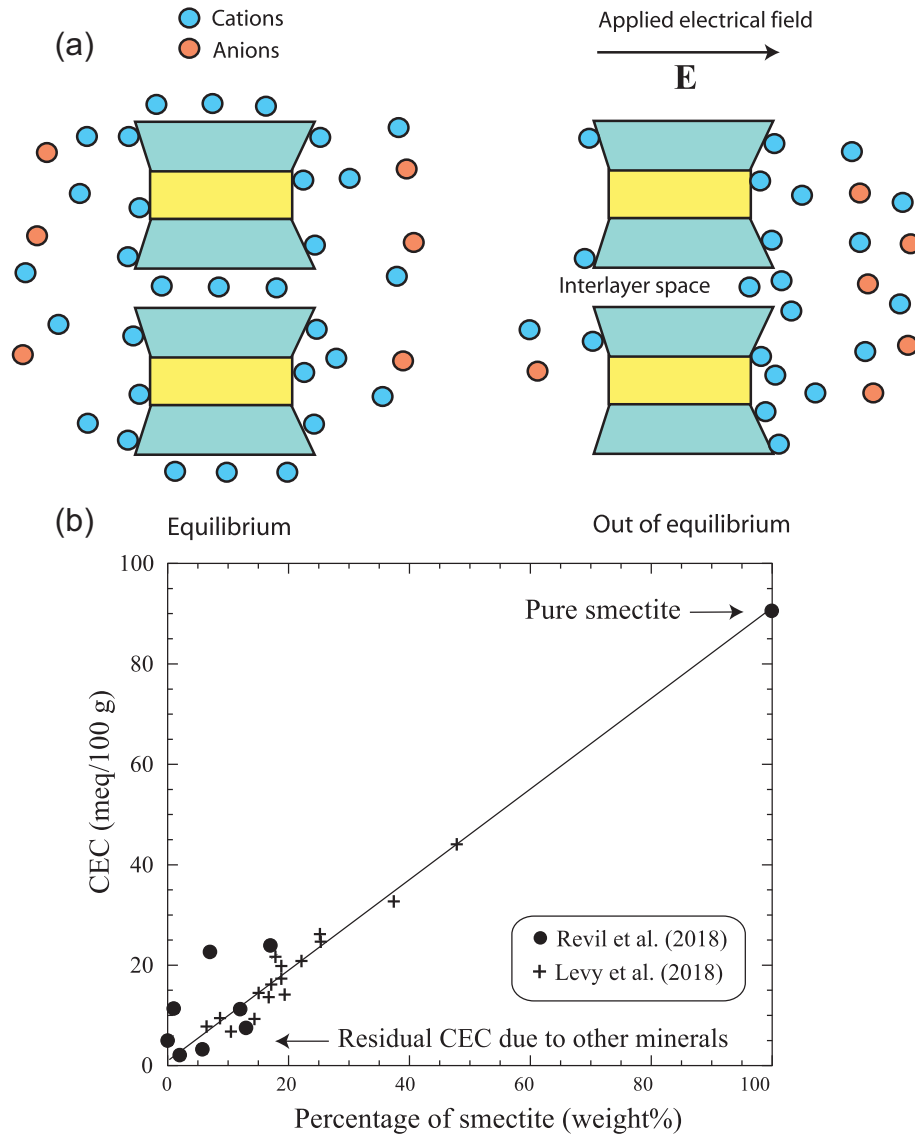
Figure 4. Polarization and conduction in smectite. (a) Conduction occurs both in the electric double layer and through the interlayer porosity. Such conduction is called 'surface conduction' at the scale of a representative elementary volume. Similarly, the polarization of smectite involves the mobilization of the ionic charge carriers of both the electrical double layer (shown in Fig. 3) and interlayer space. The migration of the cationic counterions in the direction of the electrical field lets the negative charge of the clay mineral imbalanced behind. This charge separation confers a non-dielectric dipole moment to the particle generating, in turn, a secondary electrical field. This is the essence of induced polarization. (b) Dependence of the CEC with the percentage (weight per cent) of smectite obtained from XRD measurements for volcanic rocks. We have also added the case of the pure smectite end-member. The residual CEC is due to other minerals such as clay minerals (chlorite and illite) and zeolites. This figure shows that clay-cap rich in smectite are expected to be characterized by high value of the CEC, and therefore high surface conductivity and polarization.

counter- and co-ions concentrations are controlled by Boltzmann statistics in the Coulombic field created by the mineral surface charge. We will see that this high CEC of smectite is of paramount importance to understand the conductivity and polarization of smectite-rich clay caps (Fig. 4a).

2.1 Complex electrical conductivity

Electro-diffusion processes are at the heart of induced polarization phenomena (Leroy & Revil 2009). Indeed, uder the action of an applied (primary) electrical field, ions migrate and eventually accumulate at some polarization lengths scales such as at the edges of mineral grains. If the primary field is shut down, the ions that have

accumulated want to diffuse back in their concentration field until equilibrium is again reached (Fig. 4a). In the frequency domain, induced polarization is responsible for a phase lag between the current and the electrical field. The amplitude and phase lag of the electrical conductivity can be captured by introducing a complex conductivity written as,

$$\sigma * (\omega) = \sigma' + i\,\sigma'', \tag{1}$$

where σ' and σ'' denote the in-phase and quadrature conductivity contributions, respectively. The first quantity σ' quantifies the ability of the rock to conduct current while the second quantity σ'' measures the ability of the rock to reversibly store electrical charges, that is its capacitance (Olhoeft 1985). As shown in Fig. 4(a), grains act as leaky capacitances.
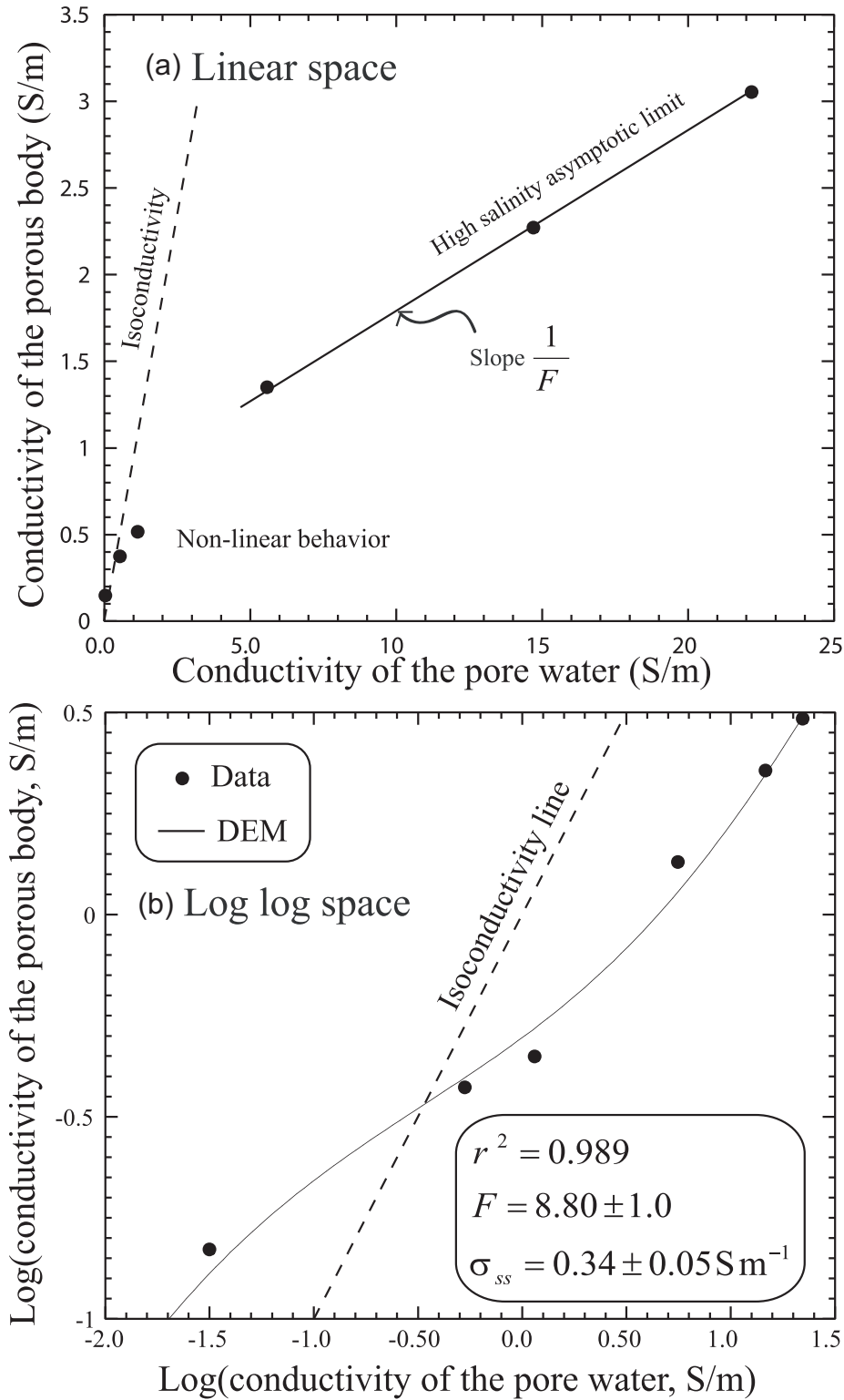
Figure 5. Conductivity curve for a soil sample (soil sample AE from Revil *et al.* 2017b). Best fit in a log–log space of the DEM (differential effective medium) used to represent the conductivity of a soil sample (sandy clay, Sample AE) as a function of the pore water conductivity. CEC = 19.1 meq/100 g and porosity 0.522 (measured). Using 1 meq/100 g = 963.20 C kg^{-1}, we obtain $Q_V = 45.5 \times 10^6$ C m^{-3} and $m = -\ln F/\ln \phi = 3.34$. (a) Linear space. (b) Log-log space. These figures show that for volcanic rocks characterized by high CEC values, the relationship between the conductivivty of the rock and the conductivity of the pore water is non-linear.

### Sandstone Sample #26 (Waxman and Smits, 1968)
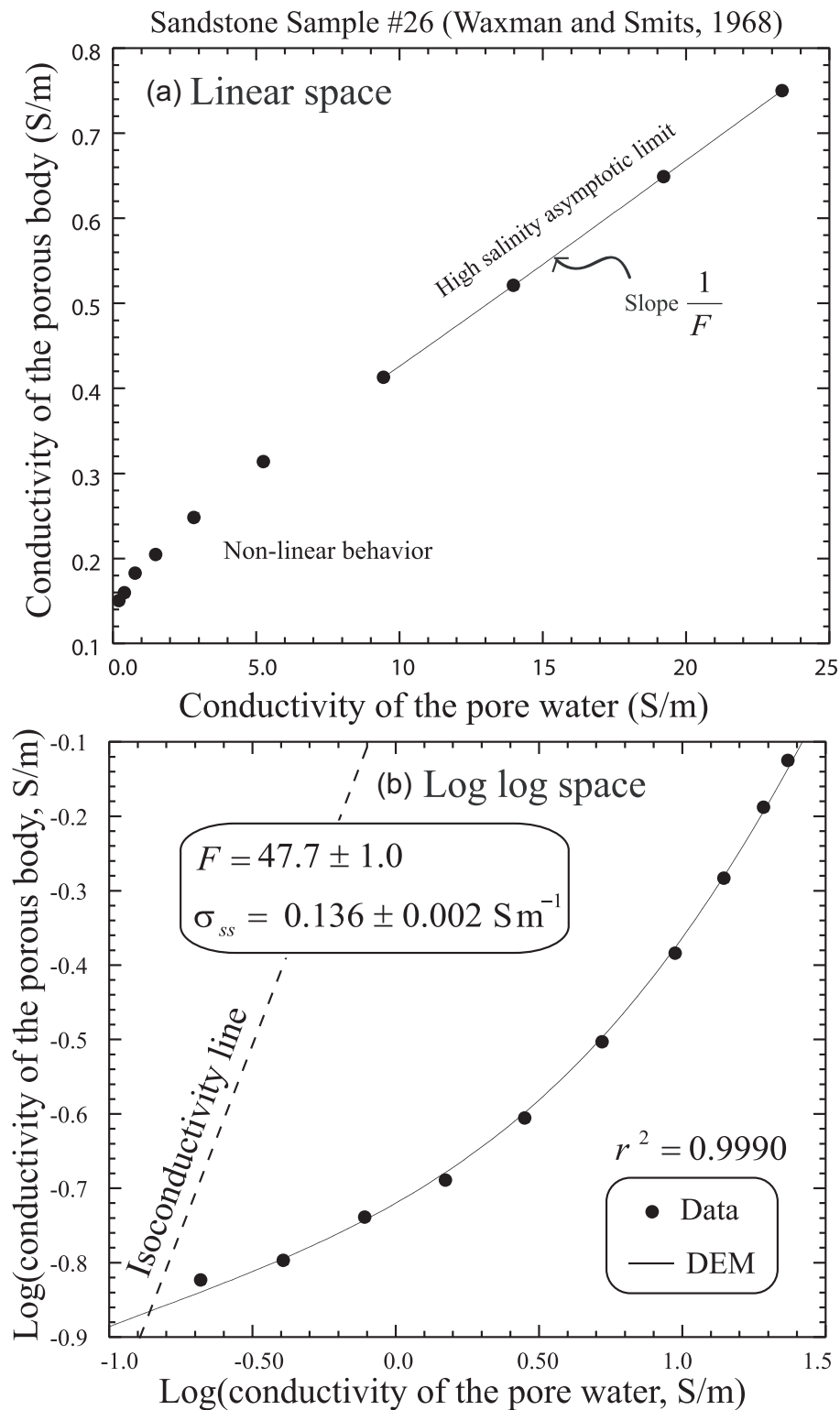
Figure 6. Best fit in a log–log space of the DEM (differential effective medium) model used to represent the conductivity of shaly sands (sample #26 from Waxman & Smits [1968](#)). The clay fraction of this sandstone is 100 per cent Montmorillonite. CEC $\approx$ 14.0 meq/100 g (porosity 0.229). The dashed line corresponds to the isoconductivity line. Using 1 meq/100 g = 963.20 C kg^{-1}, we obtain $Q_V = 120.3 \times 10^6$ C m^{-3} and $m = -\ln F / \ln \phi = 2.62$. (a) Linear space. (b) Log–log space. This figure shows the ability of the DEM approach to fit the conductivity data of smectite-rich materials.
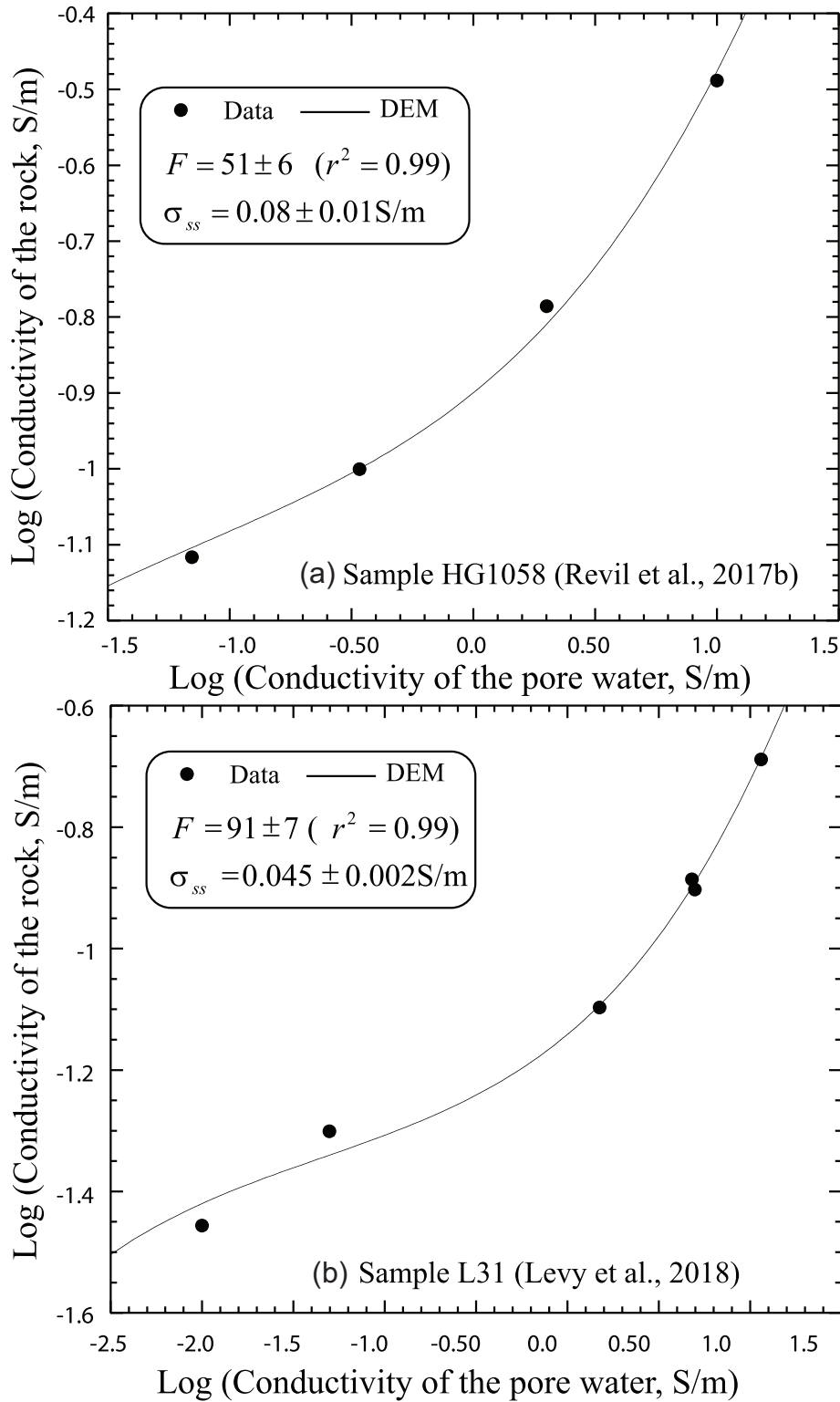
Figure 7. Electrical conductivity of volcanic rocks. (a) Conductivity sample versus pore water conductivity for the sample with the highest CEC from the study of Revil *et al.* (2017a, Sample HG1058, CEC = 23.9 meq/100 g, $\phi = 0.149$). Using 1 meq/100 g = 963.20 C kg^{-1}, we obtain $Q_V = 381 \times 10^6$ C m^{-3} and $m = -\ln F/\ln \phi = 2.07$. (b) Sample L31 from the recent study by Lévy *et al.* (2018). CEC = 32.6 meq/100 g, $\phi = 0.236$. Using 1 meq/100 g = 963.20 C kg^{-1}, we obtain $Q_V = 295 \times 10^6$ C m^{-3} and $m = -\ln F/\ln \phi = 3.12$. This figure shows the ability of the DEM approach to fit the conductivity data of volcanic rocks.
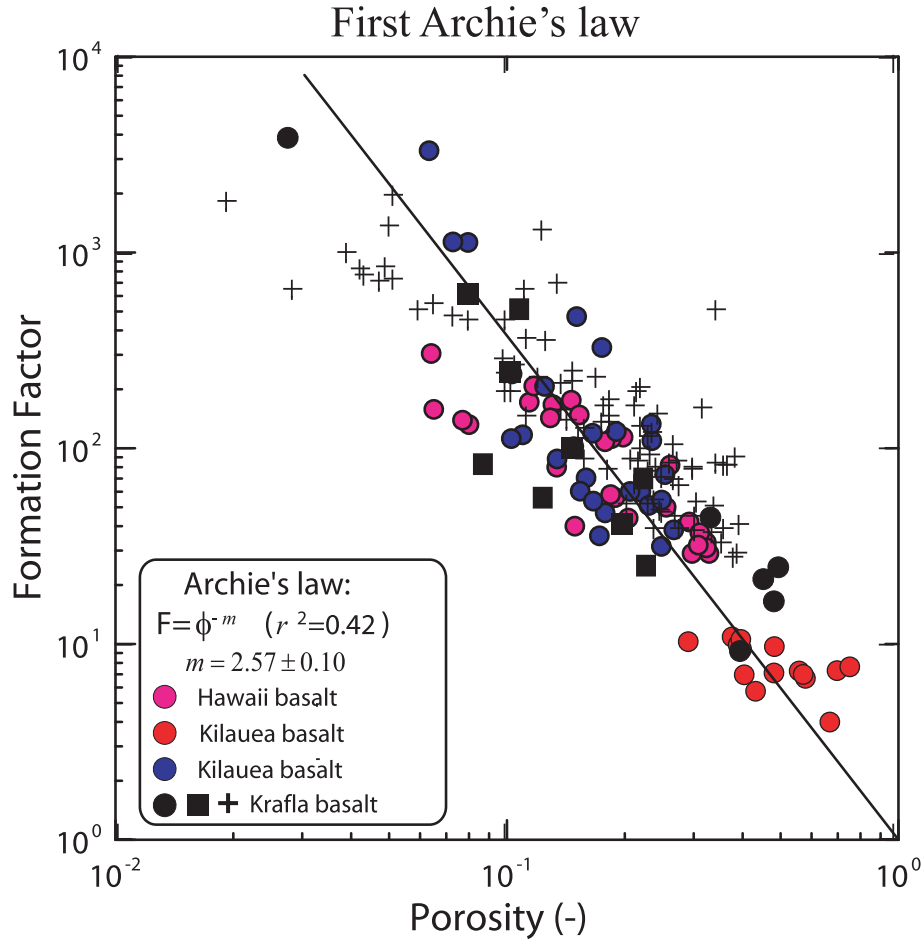
Figure 8. Key material properties controlling the electrical conductivity of volcanic rocks. (a) Formation factor versus connected porosity. The intrinsic formation factor F versus the connected porosity ϕ for the volcanic rocks of Hawaii and Kilauea (Revil *et al.* 2017d) and 10 core sample from Krafla in Iceland. Six samples corresponding to the filled circles are from the study of Revil *et al.* (2018b), nine samples corresponding to the filled squares are from the study of Flóvenz *et al.* (2005) and finally the 88 crosses are from the study of Lévy *et al.* (2018). We fit the complete data set with Archie's law $F = \phi^{-m}$ (Archie 1942) where the fitted cementation exponent is $m = 2.57 \pm 0.10$ (dimensionless). This figure provides a universal relationship for volcanic rocks between the (intrinsic) formation factor and the (connected) porosity. This relationship is of prime importance to interpret conductivity and induced polarization data in the field.

The DEM theory offers a powerful upscaling scheme to determine the effective properties of granular media (e.g. Bruggeman 1935; Hanai 1960a,b; Cosenza *et al.* 2009). The DEM model extends the linear model developed in our two previous papers (Revil *et al.* 2017a,b) to the case of high smectite contents and non-linear conductivity behaviour. The solution of the DEM scheme yields the following expression for the electrical conductivity of granular materials (e.g. Sen, Scala & Cohen 1981; Bussian 1983; Lima & Sharma 1990),

$$\sigma^* = \sigma_w \phi^m \left(\frac{1 - \frac{\sigma_{ss}^*}{\sigma_w}}{1 - \frac{\sigma_{ss}^*}{\sigma^*}} \right)^m, \tag{2}$$

where σ_w (in S m^{-1}) denotes the conductivity of the pore water, ϕ (dimensionless) denotes the connected porosity, m (dimensionless) is the porosity exponent of Archie's law (cementation exponent) and where the complex and frequency-dependent grain conductivity σ_{ss}^* (S m^{-1}) is given by (Niu & Revil 2016)

$$\sigma_{ss}^*(\omega) = \sigma_{ss}^\infty - (\sigma_{ss}^\infty - \sigma_{ss}^0) \int_0^\infty \frac{h(\tau)}{1 + (i\omega\tau)^{1/2}} d\tau, \tag{3}$$

where σ_{ss}^∞ and σ_{ss}^0 denote the instantaneous and dc grain conductivity (see discussion in Ghorbani *et al.* 2018, for volcanic rocks), $h(\tau)$ denotes a normalized probability density (kernel) for the relaxation times τ, which can be related in turn to the grain sizes or the pore sizes (Revil & Florsch 2010; Niu & Revil 2016). The grain conductivity should not be mixed with the surface conductivity that will be defined below; they are however proportional to each other. In this paper, we will not discuss further the relaxation times or the relaxation time distribution. We just assume this distribution to be broad enough (over 3 orders of magnitude) and consequently the in-phase and quadrature conductivity spectra are rather flat leading to the so-called constant phase model (Vinegar & Waxman 1984; Revil *et al.* 2017c).

One of the key intrinsic induced polarization parameters is the normalized chargeability (). The normalized chargeability (in S m^{-1}) is defined as,

$$M_n = \sigma_\infty - \sigma_0, \tag{4}$$

where σ_∞ and σ_0 denote the instantaneous and dc-conductivity of the rock, respectively. The chargeability (dimensionless) is defined as $M = M_n/\sigma_\infty$. The introduction of this terminology for the normalized chargeability (in S m^{-1}) may seem inappropriate. In
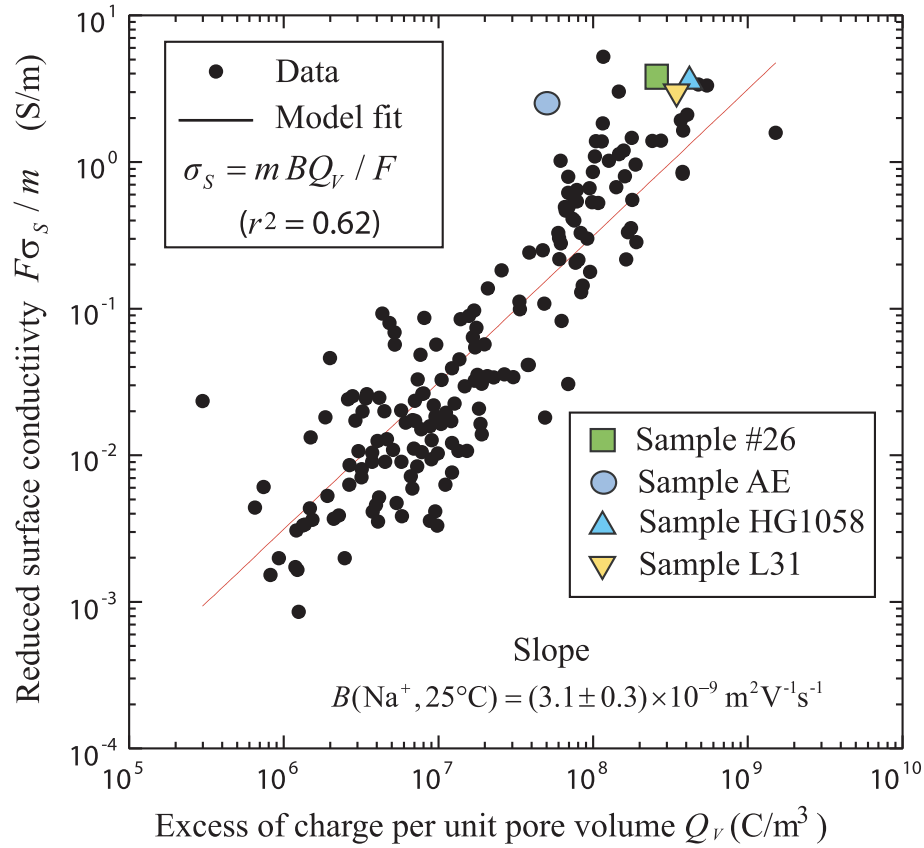
Figure 9. Reduced surface conductivity (defined as the ratio $F\sigma_S/m$ in which σ_S denotes the surface conductivity) versus the excess of charge per unit pore volume determined from the porosity and the CEC. The trend is fitted according to a linear trend passing through the origin of the coordinates. The slope represents the apparent mobility of the counterions B entering the equation of the surface conductivity. This figure provides a universal relationship for volcanic rocks between the (reduced) surface conductivity and the excess of charge per unit pore volume determined from the CEC and the porosity. This relationship is of prime importance to interpret conductivity and induced polarization data in the field.

hydrogeophysics however, it is common to normalize chargeability by resistivity *to remove* the fingerprint of resistivity on the inverted chargeability tomograms (see discussions in Slater & Glaser 2003). This is the chargeability that is directly imaged in time-domain induced polarization but the normalized chargeability is the property of interest in petrophysics for the reasons that will be exposed below. The instantaneous conductivity describes the conductivity right away after the introduction of a primary electrical field (transient electromagnetic induction effects being neglected). All the charge carriers are mobile. The dc conductivity corresponds to the conductivity measured after a long application of the electrical field (i.e. much a time longer than the relaxation times contained in the relaxation time distribution $h(\tau)$). Some of the charge carriers are not available anymore for polarization because they have accumulated at some polarization length scales (such as the grain size in Fig. 4a). The difference between the two conductivities is due to the dispersion of the conductivity curve (i.e. its variation with the frequency), which is itself associated through the Kramers–Kronig relationships with the existence of the quadrature conductivity and hence polarization (de Kronig 1926; Kramers 1927; de Kronig 1942). We assume below that the influence of semi-conductors (pyrite, magnetite) can be safely ignored at least for the altered volcanic rocks (see Ghorbani *et al.* 2018, for an extended discussion on this subject).

2.2 Instantaneous electrical conductivity

From eq. (2), we can extract the instantaneous conductivity σ_∞ of the porous material as a function of the instantaneous conductivity of the solid phase σ_{ss}^∞ (e.g. Bussian 1983)

$$\sigma_\infty = \sigma_w \phi^m \left(\frac{1 - \frac{\sigma_{ss}^\infty}{\sigma_w}}{1 - \frac{\sigma_{ss}^\infty}{\sigma_\infty}} \right)^m. \tag{5}$$

In absence of grain conductivity, i.e. for $\sigma_{ss} = 0$, we recover Archie's (1942) definition of the formation factor:

$$\lim_{\sigma_{ss}^\infty \to 0} \sigma_\infty = \frac{\sigma_w}{F}, \tag{6}$$

where $F = \phi^{-m}$ denotes the first Archie's law (Archie 1942). The first Archie's law is valid whatever the grain conductivity values. In saturated conditions and above the so-called isoconductivity point (i.e. for $\sigma_w \leq \sigma_\infty^\infty$), the grain conductivity is dominated by the conductivity of the smectite particles and their CEC. Revil *et al.* (2018a) showed that the grain conductivity can be related to their volumetric charge density Q_V by

$$\sigma_{ss}^\infty \approx \frac{1}{F} B Q_V, \tag{7}$$

where B ($m^2 s^{-1} V^{-1}$) denotes the apparent mobility of the counterions in the double layer (actually a composite of the mobility of the
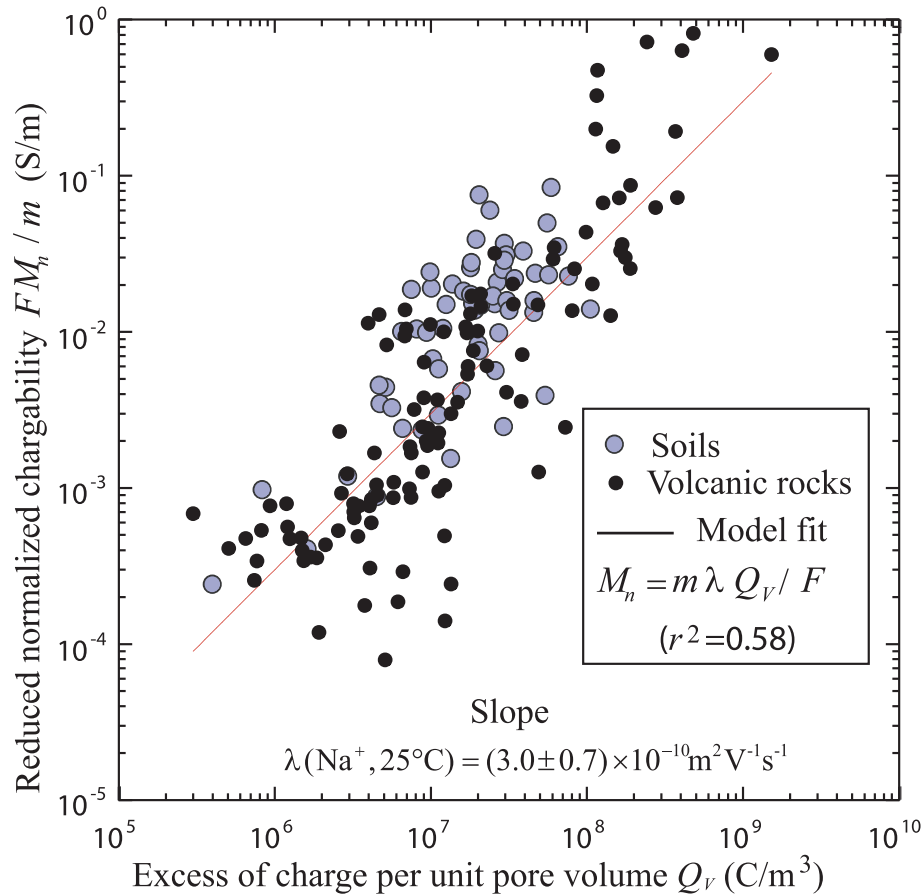
Figure 10. Reduced normalized chargeability versus the excess of charge per unit pore volume determined from the porosity and the CEC. The trend is fitted according to a linear trend passing through the origin of the coordinates. The slope represents the apparent mobility of the counterions λ entering the equation of the normalized chargeability. The filled circles correspond to the data from the following papers: Revil *et al.* (2017a,b), and Ghorbani *et al.* (2018). The data from the soils are from Revil *et al.* (2017c). This figure provides a universal relationship for volcanic rocks between the (reduced) normalized chargeability and the excess of charge per unit pore volume. This relationship is of prime importance to interpret conductivity and induced polarization data in the field.

counterions in the Stern layer and in the diffuse layer, Fig. 3c), and where the total volumetric charge density Q_V (in C m^{-3}) is written as a function of the CEC as (e.g. Waxman & Smits 1968),

$$Q_V = \rho_g \left(\frac{1-\phi}{\phi} \right) \text{CEC}, \tag{8}$$

where the CEC is expressed in C kg^{-1} (1 meq/100 g = 963.20 C kg^{-1}) and ρ_g denotes the mass density of the grains (typically between ~3000 kg m^{-3} for volcanic rocks). The CEC of the rock can be written as a function of the weight content of smectite as (Revil *et al.* 1998, 2002b)

$$\text{CEC} = \varphi_W(S)\text{CEC}(S) + [1 - \varphi_W(S)]\,\text{CEC}_r, \tag{9}$$

where CEC(S) denotes the CEC of smectite (approximately 80–100 meq/100 g, for example Waxman & Smits 1968), $\varphi_W(S)$ denotes the weight fraction of smectite (including the mass fraction of smectite in the mixed layer clays), and CEC$_r$ denotes the residual CEC associated with the other minerals such as illite, chlorite and zeolites. Eq. (5) has the following closed-form solution (Revil *et al.* 1998; Revil 2000),

$$\sigma_\infty \approx \frac{\sigma_w}{F}\left[FX_\infty + \frac{1}{2}(1 - X_\infty)\left(1 - X_\infty + \sqrt{(1 - X_\infty)^2 + 4FX_\infty}\right)\right], \tag{10}$$

where the (high frequency) Dukhin number (dimensionless) is defined by (Revil *et al.* 1998),

$$X_\infty \equiv \frac{\sigma_{ss}^\infty}{\sigma_w}. \tag{11}$$

A high salinity asymptotic limit ($X_\infty \ll 1$) can be obtained directly from eq. (5) using Newton binomial expansion (Bussian 1983)

$$\sigma_\infty \approx \frac{\sigma_w}{F} + m\,\sigma_{ss}^\infty. \tag{12}$$

So the surface conductivity σ_S^∞ defined in Waxman & Smits (1968) as $\sigma_\infty = \sigma_w/F + \sigma_S^\infty$ is related to the grain conductivity by $\sigma_S^\infty = m\,\sigma_{ss}^\infty$ Note that for $X_\infty = 1$ (defining the isoconductivity point), eq. (5) yields,

$$\sigma_\infty(X_\infty = 1) = \sigma_w = \sigma_{ss}^\infty. \tag{13}$$

In other words, the isoconductivity point is characterized by an equality between the (instantaneous) conductivity of the medium filled with pore water and the conductivity of the solid phase (smectite grains) coated by the electrical double layer. Below the isoconductivity point (i.e. $\sigma_w \leq \sigma_{ss}^\infty$), eq. (5) can be also be written as (see details in Revil *et al.* 2018a),

$$\sigma_\infty = \sigma_w \phi^{\frac{m}{1-m}} \left(\frac{1 - \sigma_w/\sigma_{ss}^\infty}{1 - \sigma_\infty/\sigma_{ss}^\infty} \right)^{\frac{m}{1-m}}. \tag{14}$$
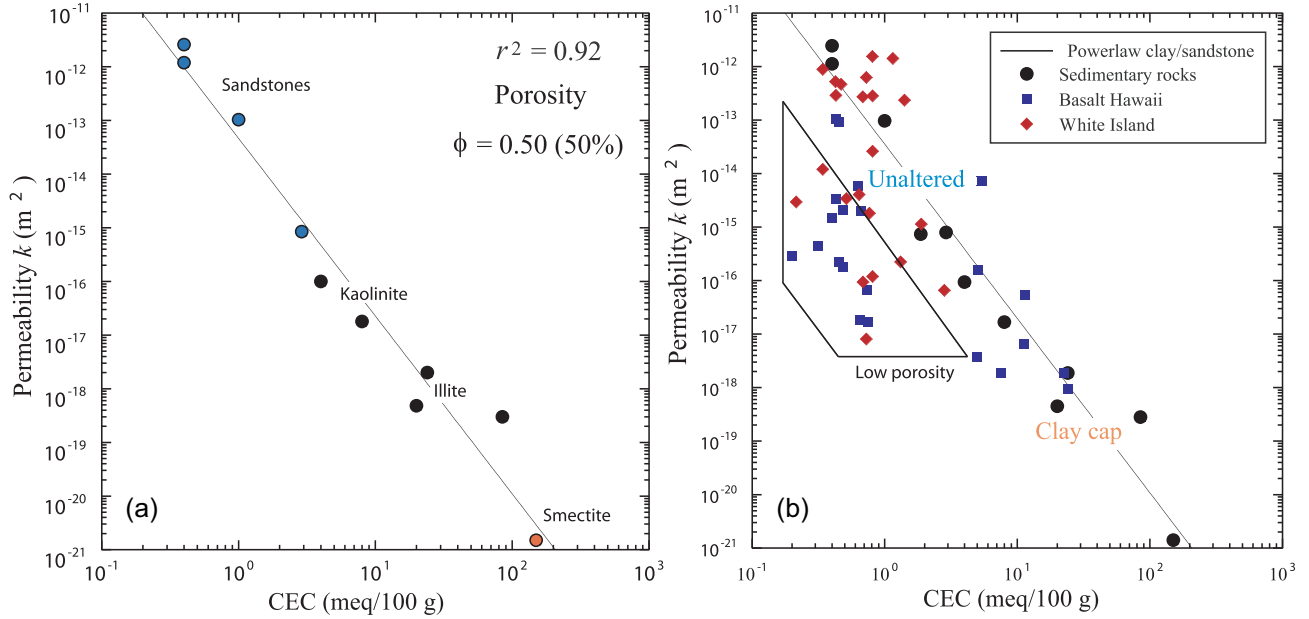
Figure 11. Permeability as a function of the CEC. (a) Trend at constant porosity (0.50 for the samples except for the sandstones which are at an average porosity of 0.20). Data are from: Mesri & Olson (1971) (illite, smectite, kaolinite at 50 per cent porosity), Horpibulsuk et al. (2011) (bentonite, kaolinite, Bangkok clay, porosity at 50 per cent) and the other data are from Howard (1992) (sandstones at 20 per cent porosity). This relationship implies that if the CEC can be determined in the field by using conductivity and induced polarization imaging, its values can be used to determine the permeability of the clay cap. (b) Permeability as a function of the CEC (here expressed in meq/100 g) for the porosity range (0.30–0.60). Data from: Sedimentary rocks and clays, plus the Portland sandstone data from Niu et al. (2016). The volcanic rocks from Hawaii are from the study by Revil et al. (2017b). The data from White Islands are from Ghorbani et al. (2018) with the permeability data originally from Heap et al. (2017). This relationship implies that the permeability of rock formations can be determined from electrical conductivity and induced polarization imaging.

A low-salinity closed-form solution of eq. (14) for the instantaneous electrical conductivity is obtained by taking the root of eq. (14) when $m \sim 2$ in the power of the argument in parenthesis in eq. (14) (see Revil 2000, for a complete demonstration). This closed-form solution is,

$$\sigma_\infty \approx \frac{\sigma_w}{g} \left[g X_\infty + \frac{1}{2}(1 - X_\infty)\left(1 - X_\infty + \sqrt{(1 - X_\infty)^2 + 4 g X_\infty}\right)\right],$$
(15)

with a low salinity formation factor $g = \phi^{m/(1-m)} = F^{1/(m-1)} \geq 1$ (with $m = 2$, $g = F$). When surface conductivity dominates, we obtain

$$\lim_{X \gg 1} \sigma_\infty = g\sigma_w \left[1 + O(X_\infty^{-1})\right],$$
(16)

$$\lim_{X_\infty \gg 1} \left(\frac{1}{\sigma_\infty}\right) = \frac{1}{g\sigma_w}\left[1 + \frac{m}{m-1}(g-1)\frac{1}{X_\infty} + O(X_\infty^{-2})\right],$$
(17)

where eq. (17) can also be obtained directly from eq. (14) using Newton binomial expansion (Lima & Sharma 1990). In these equations 'O' (Big O) denotes the Bachmann–Landau notation for the expansion describing the limiting behaviour of a function when the argument tends towards a particular value.

Similar expressions can be derived for the dc conductivity σ_0 by substituting X_∞ by X_0

$$X_0 = \frac{\sigma_{ss}^0}{\sigma_w} \approx \frac{1}{F\sigma_w}(B - \lambda)Q_V,$$
(18)

in eq. (10). In eq. (18) λ (in $m^2 V^{-1} s^{-1}$) denotes the mobility associated with the Stern layer (e.g. Vinegar & Waxman 1984). The mobilities B and λ can be related to the intrinsic mobilities of the

counterions in the diffuse and Stern layers shown in Fig. 3 (see Revil et al. 2017a and Ghorbani et al. 2018 for instance for further details).

The dependence of the instantaneous conductivity on the temperature is controlled by the influence of this parameter on both the conductivity of the pore water and the mobility B through eqs (7), (10) and (11). The temperature dependence of these to quantities can be modeled by an Arrhenius equation (e.g. Soueid Ahmed et al. 2018; Ghorbani et al. 2018),

$$\sigma_w(T) = \sigma_w(T_0)\exp\left[-\frac{E_a}{k_b N}\left(\frac{1}{T} - \frac{1}{T_0}\right)\right],$$
(19)

$$B(T) = B(T_0)\exp\left[-\frac{E_a}{k_b N}\left(\frac{1}{T} - \frac{1}{T_0}\right)\right],$$
(20)

where T and T_0 are expressed in degree Kelvin (K) ($T_0 = 298$ K) denotes the reference temperature, that is 25 °C), $k_b N = 8.314$ J mol^{-1} K^{-1}), $E_a = 16$ kJ Mol^{-1}, $\sigma_w(T_0)$ depends on the salinity, and the value of $B(Na^+, 25$ °C) will be determined below. The temperature dependence of the mobility $\lambda(T)$ entering the dc conductivity (and the normalized chargeability, see next section) is also modeled by an Arrhenius equation,

$$\lambda(T) = \lambda(T_0)\exp\left[-\frac{E_a}{k_b N}\left(\frac{1}{T} - \frac{1}{T_0}\right)\right],$$
(21)

where $E_a = 16$ kJ Mol^{-1} and $\lambda(Na^+, 25$ °C) will be determined below from a comparison between the data and the model (Ghorbani et al. 2018). The other parameters m, Q_V, CEC and ϕ entering our model are temperature independent for a given porous material.
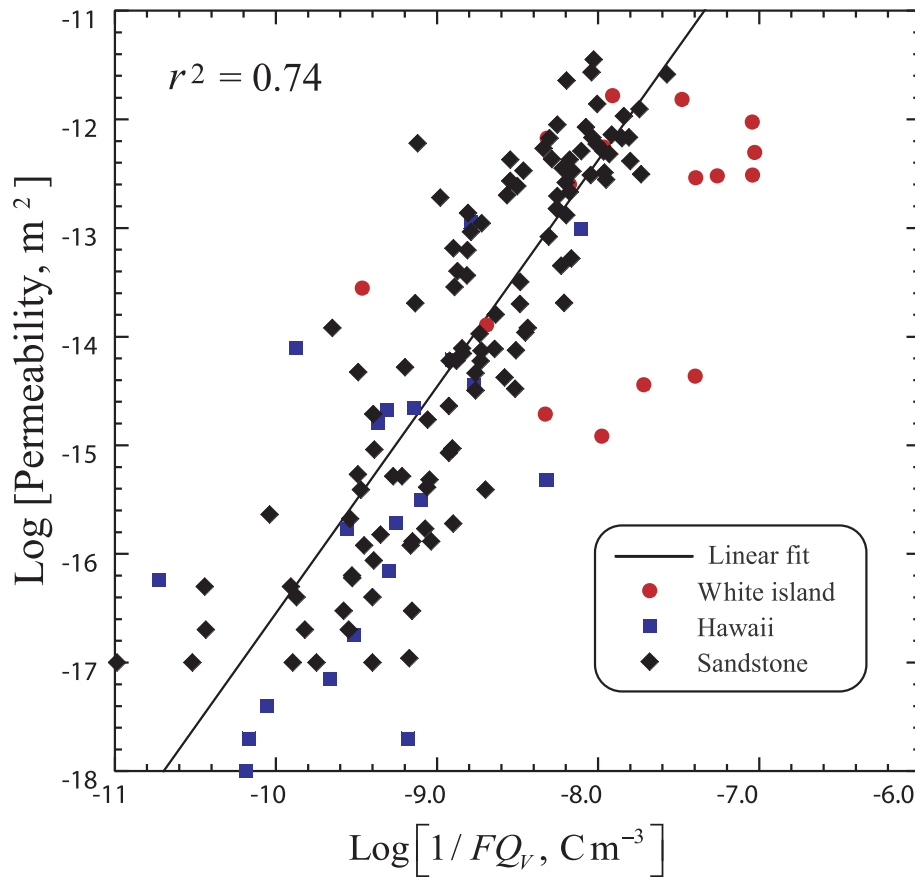
Figure 12. Permeability as a function of the inverse of the ratio of the product of the formation factor F by the volumetric charge density Q_V. Data from: Niu *et al.* (2016) (Portland sandstone), Revil *et al.* (2017b, Hawaiian basalts), Ghorbani *et al.* (2018) and Heap *et al.* (2017) (volcanic rocks from White Islands), and Sen *et al.* (1990) (sandstones). The dependence described in the main txt captures both the effect of the porosity and the CEC. The linear fit (least-square regression) yields $k = 10^{4.30} (1/FQ_V)^{2.09}$ ($r^2 = 074$). This relationship implies that the permeability of rock formations can be determined from electrical conductivity and induced polarization imaging like in Fig. 11(b).

2.3 Normalized chargeability

Starting with the definition of the normalized chargeability, eq. (4), we obtain the following expression of the normalized chargeability in the high salinity non-linear regime (i.e. above the isoconductivity point) as,

$$M_n \approx \frac{\sigma_w}{F}\left[\begin{array}{c} F(X_\infty - X_0) + \frac{1}{2}(1 - X_\infty)\left(1 - X_\infty + \sqrt{(1 - X_\infty)^2 + 4FX_\infty}\right) \\ -\frac{1}{2}(1 - X_0)\left(1 - X_0 + \sqrt{(1 - X_0)^2 + 4FX_0}\right) \end{array}\right]. \tag{22}$$

In the high salinity (superscript HS) asymptotic linear regime, eq. (12) (and a similar expression for the dc conductivity) taken together with eq. (4) yield the following expression for the normalized chargeability,

$$M_n \approx m(\sigma_{ss}^\infty - \sigma_{ss}^0), \tag{23}$$

$$M_n^{HS} \approx m\frac{1}{F}\lambda Q_V. \tag{24}$$

Similar equations can be obtained for the low salinity (superscript LS) regime. The asymptotic behaviour (using eq. 16) of the normalized chargeability at very low salinities is

$$M_n^{LS} \approx 0. \tag{25}$$

Therefore the normalized chargeability is an increasing function of the pore water conductivity until a constant asymptotic limit is reached at high salinity and is null at low salinities. The reason of this behaviour are discussed in Revil *et al.* (2018a, their fig. 14b) is that at very low salinities (i.e. much below the isoconductivity point), the electrical field avoids the grains and their electrical double layer and therefore cannot polarize them.

In the high salinity limit, the relationship of the normalized chargeability to the surface conductivity is given by

$$\frac{M_n^{HS}}{\sigma_S^\infty} = \frac{\lambda}{B} = R, \tag{26}$$

where R is a dimensionless universal constant on the order of 8 to 10×10^{-2} independent of the temperature and water content (since B and λ have the same temperature and water content dependences, e.g. Ghorbani *et al.* 2018).
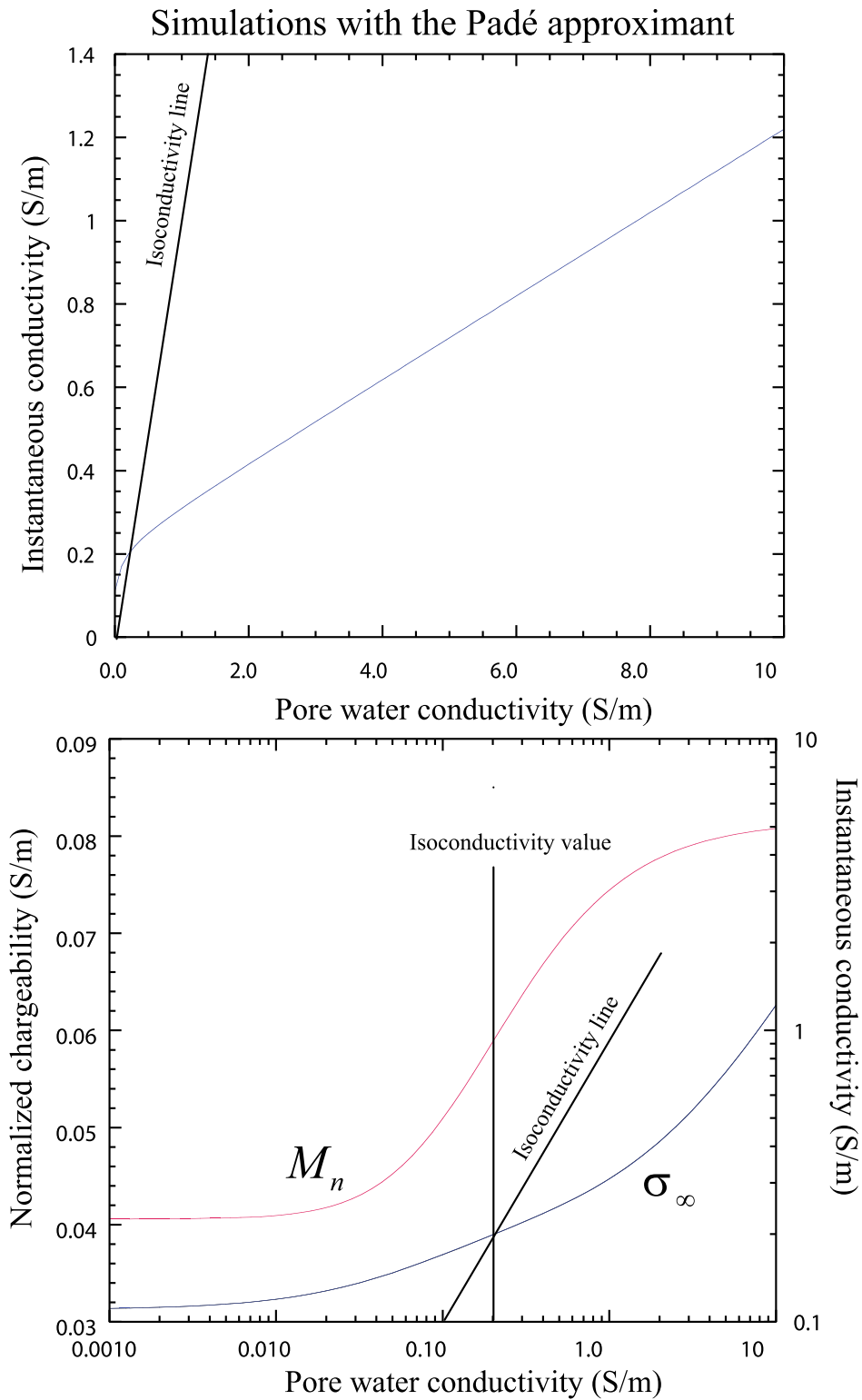
2.3 Prediction of permeability

One of the key goal in hydrogeophysics is to image permeability thanks to geophysical methods (e.g. Binley *et al.* 2015). This is always a challenging task since the permeability can vary over 12 orders of magnitudes in rocks and soils. Revil *et al.* (2002) showed that at a constant porosity, the permeability follows a power-law relationship with the CEC:

$$k = k_0 \mathrm{CEC}^{-b}, \tag{27}$$
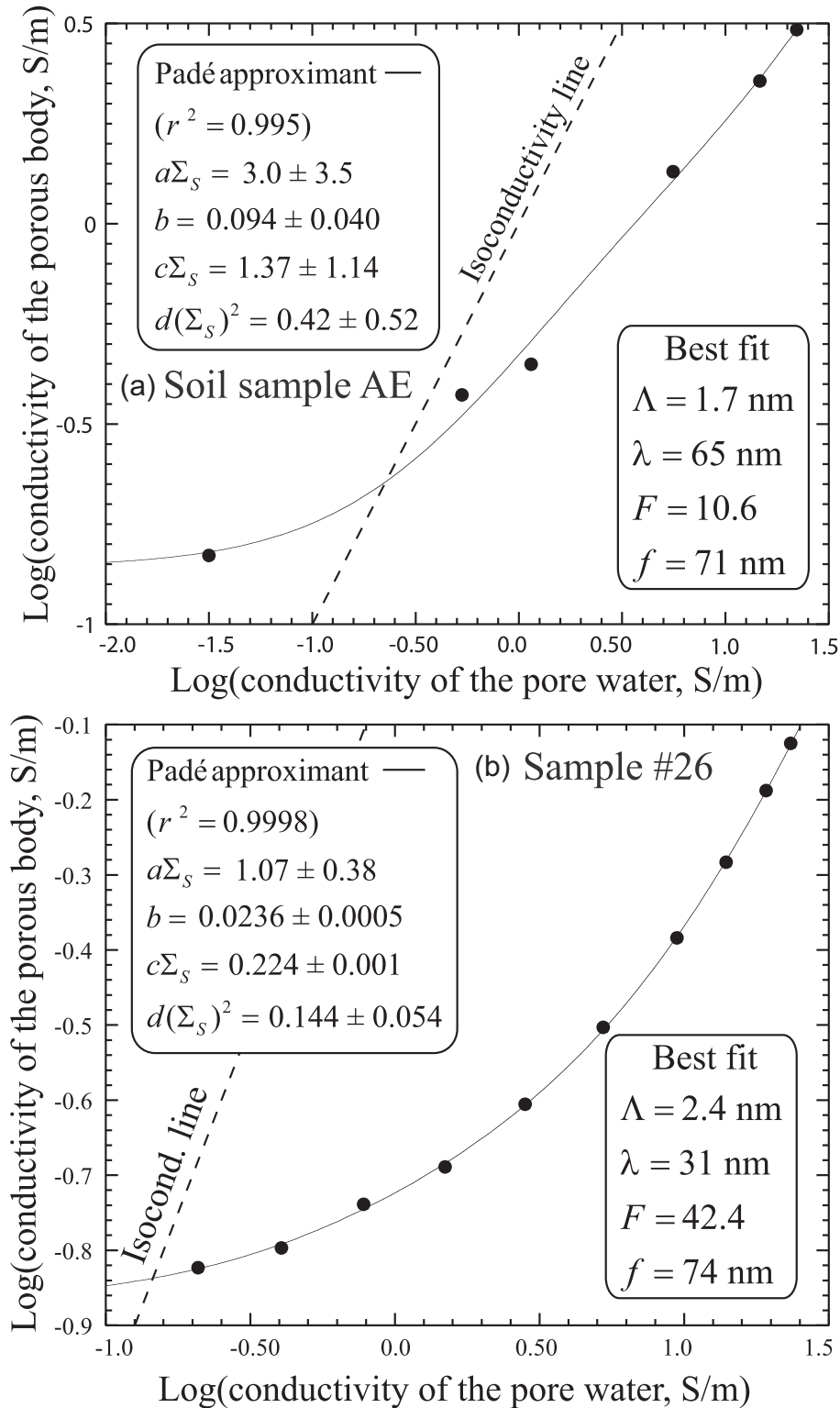
Figure 13. Application of the volume averaging model. (a) Conductivity curve for a soil sample (data from Revil *et al.* 2017b). Best fit in a log–log space of the Padé approximant used to represent the conductivity of a soil sample (sandy clay) as a function of the pore water conductivity. CEC = 19.3 meq/100 g (porosity 0.522). (b) Best fit in a log-log space of the Padé approximant to fit the data of sample #26 from Waxman & Smits (1968). The clay fraction of this sandstone is 100 per cent Montmorillonite. CEC ≈ 14.0 meq/100 g (porosity 0.229). These figures imply that the volume-averaging model is also able to capture the non-linearity between the conductivity of the rock and the conductivity of the pore water for smectite-rich rocks.

Figure 14. Simulation of the instantaneous conductivity σ_∞ and normalized chargeability M_n as a function of the pore water conductivity for the four textural parameters discussed in the main text. The plain lines correspond to the predictions of the volume averaging approach using salinity-independent specific surface conductivities.
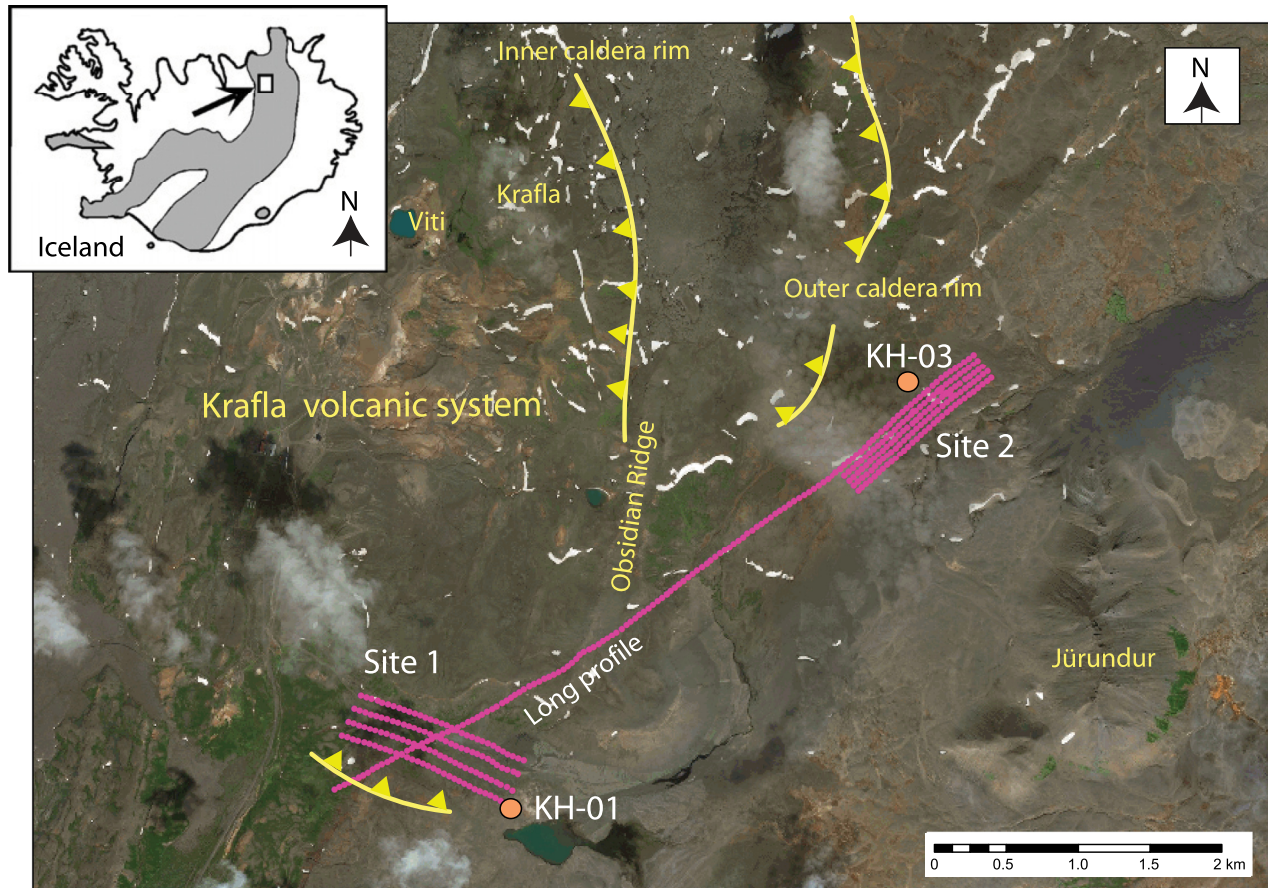
Figure 15. Localization of the Krafla caldera in Iceland. The map shows also the approximate position of the Krafla caldera according to Jónasson (1994) and the two test sites labeled as Site 1 and Site 2 and the position of the two boreholes where the temperature is measured. The dots correspond to the position of the electrodes. Insert: position of Krafla in Iceland. The grey areas correspond to the Northern Volcanic Zone (NVZ), Eastern Volcanic Zone (EVZ) and Western Volcanic Zone (WVZ).

where k_0 and b will be determined below and the CEC is expressed in meq/100 g. Eq. (27), however, does not capture the influence of the porosity upon the permeability. Sen *et al.* (1990) proposed the following relationship,

$$k = k_0(1/FQ_V)^c, \tag{28}$$

where k_0 and c are two fitting parameters. Eq. (28) extends an equation proposed by Goode & Sen (1988) in which the permeability was predicted from Q_V.

2.4 Comparison with experimental data

First, we check the relationship between the CEC and the smectite content of volcanic rocks (Fig. 4b) and a comparison with made with the prediction of eq. (9). Since the CEC of smectite is much larger than the CEC of other clay materials, it is not surprising that a small amount of smectite dominates the CEC response of the whole material.

We check now if the proposed model can explain the non-linearity of the conductivity curve. We first fit two data sets on soils (Fig. 5) and a sandstone (Fig. 6), both rich in smectite. In both cases, the non-linear model is able to fit the data. We use two volcanic core samples characterized by very high CEC values (from the studies by Revil *et al.* 2017b, and Lévy *et al.* 2018, Fig. 7). Our model is able to capture the non-linear behaviour of the conductivity data with only two fitting parameters.

There are two predictions of our DEM model we can further test regarding the dependence of the surface conductivity and normalized chargeability with the CEC: (1) The product of the formation factor by the grain conductivity (divided by the porosity exponent m) is linearly related to the excess of charge per unit pore volume (indeed $\sigma_S^\infty = m\,\sigma_{ss}^\infty$ and σ_{ss}^∞ is given by eq. 7). (2) The product of the formation factor by the normalized chargeability (divided by the porosity exponent m) is linearly related to the excess of charge per unit pore volume (see eq. 24). We first plot the intrinsic formation factor as a function of the connected porosity (Fig. 8). The intrinsic formation factor and grain conductivity are determined by fitting eq. (10) to the conductivity data obtained at different salinities. The data are fitted by using Archie's law and we obtain $m = 2.57$ (Fig. 8), a value that will be used below.

To test the two predictions discussed above, we use the database of 205 core samples: 27 samples from Kilauea (Hawaii, see Revil *et al.* 2017a,b), 42 samples from Kilauea (unpublished), 16 samples from Papadayan volcano and 16 samples from Merapi volcano, both in Indonesia (Ghorbani *et al.* 2018), 5 samples from Furnas volcano (Azores Islands, Portugal, Ghorbani *et al.* 2018), 50 samples from Yellowstone (Ghorbani *et al.* 2018), 22 samples from White Island volcano (Ghorbani *et al.* 2018), 6 samples from Krafla (unpublished) and 21 volcaniclastic samples rich in zeolites (Revil *et al.* 2002). The slope of the linear trend between the reduced surface conductivity and the excess of charge data can be used to determine the value

(a) Time series in induced polarization

(b) Spatial configuration
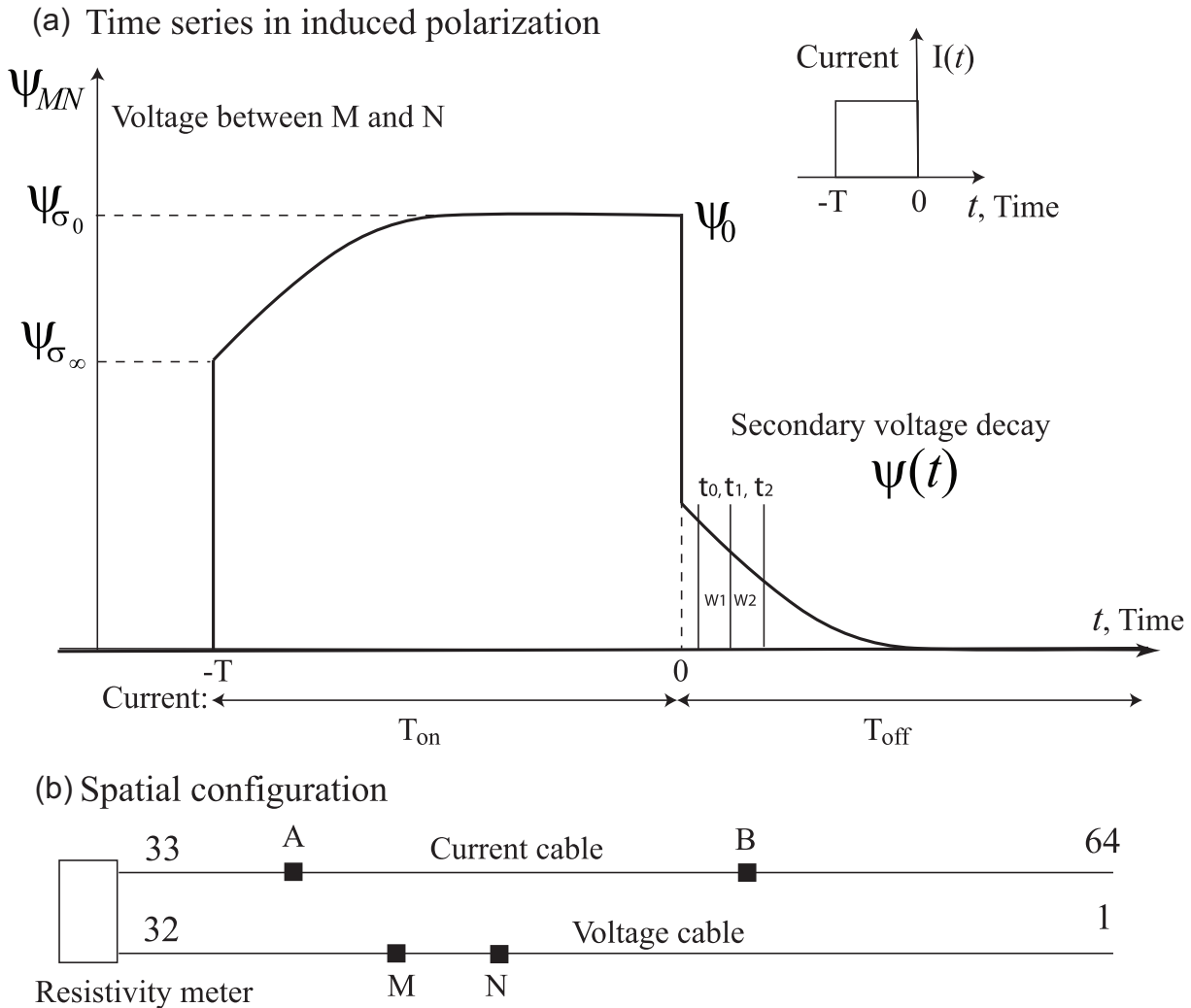
Figure 16. Acquisition of the time-domain induced polarization data. (a) The primary current injected in the ground between electrodes A and B corresponds to a box signal of period T. The potential difference between the voltage electrodes M and N is the sum of a primary voltage ψ_∞ and a secondary voltage ψ_0-ψ_∞. Once the primary current is shut down (for $t > 0$), only the secondary voltage persists and is decaying over time while the charge carriers are coming back to their equilibrium position (see Fig. 4a). This decaying secondary voltage is measured into windows (W_1, W_2, etc.) separated by characteristic times ($t_0, t_1, t_2, \ldots$). The partial chargeabilities are determined for each of these windows by integrating the secondary voltage over time. The chargeability can be defined as (ψ_0-ψ_∞)/ψ_0. (b) Spatial configuration for the induced polarization measurements. We used two sets of 32 electrodes for the current and voltage electrodes. These two sets are located on two distinct cables (each 1240-m-long). The numbers 1–64 correspond to the labels of the electrodes in the protocol.

of $B(\text{Na}^+, 25\,^\circ\text{C})$. We obtain $B(\text{Na}^+, 25\,^\circ\text{C}) = 3.1 \pm 0.3 \times 10^{-9}$ $\text{m}^{-2}\text{s}^{-1}\text{V}^{-1}$ (Fig. 9). The slope of the linear trend can be used to determine the value of $\lambda(\text{Na}^+, 25\,^\circ\text{C})$. We obtain $\lambda(\text{Na}^+, 25\,^\circ\text{C}) = 3.0 \pm 0.7 \times 10^{-10}$ $\text{m}^{-2}\text{s}^{-1}\text{V}^{-1}$ (Fig. 10). The dimensionless number entering eq. (27) is given by $\lambda/B = R = 0.10$, close to the value obtained in Ghorbani *et al.* (2018) (8×10^{-2}).

Finally, we test the permeability predictors developed above. We correlate the permeability as a function of the CEC for different types of clays and sandstones (Fig. 11a). For a porosity of $\sim$0.50, the permeability is very dependent on the CEC. A power law fit (least square regression) applied to these data yields $k = 10^{-13.3}\,\text{CEC}^{-3.3}$ ($r^2 = 0.92$) where the CEC is expressed in meq/100 g. Permeability is therefore a very strong function of the CEC of the material. This is because the inverse of the CEC can be used as a proxy or the pore size (Revil *et al.* 2002b, see Fig. 11b). To go one step further, we test the validity of eq. (28). We see that eq. (28) captures the combined effects of the porosity and CEC (in reality F and Q_V) upon the permeability (Fig. 12). A linear fit (least square regression) applied

to the data yields $k = 10^{4.30}\,(1/FQ_V)^{2.09}$ ($r^2 = 074$) where Q_V is expressed in C m^{-3}.

3 VOLUME AVERAGING THEORY

As mentioned above, non-linear behaviours between the rock conductivity and the pore water conductivity were recognized from very early (e.g. van Olphen & Waxman 1958; Gast 1966; Jorgensen & Low 1970; Shainberg & Levy 1975). These evidences prompted the development of a specific non-linear conductivity model in geophysics called the 'three layers resistor model' by Wyllie & Southwick (1954). The three layers resistor model has since being extensively used and discussed in the literature (Sauer *et al.* 1955; Spiegler *et al.* 1956; Gast 1966; Bussian 1983; Mitchell 1993; Lima *et al.* 2010) and extended to partially saturated media by Rhoades *et al.* (1989) and Revil *et al.* (2018a). Fig. 1 by Rhoades *et al.* (1989)
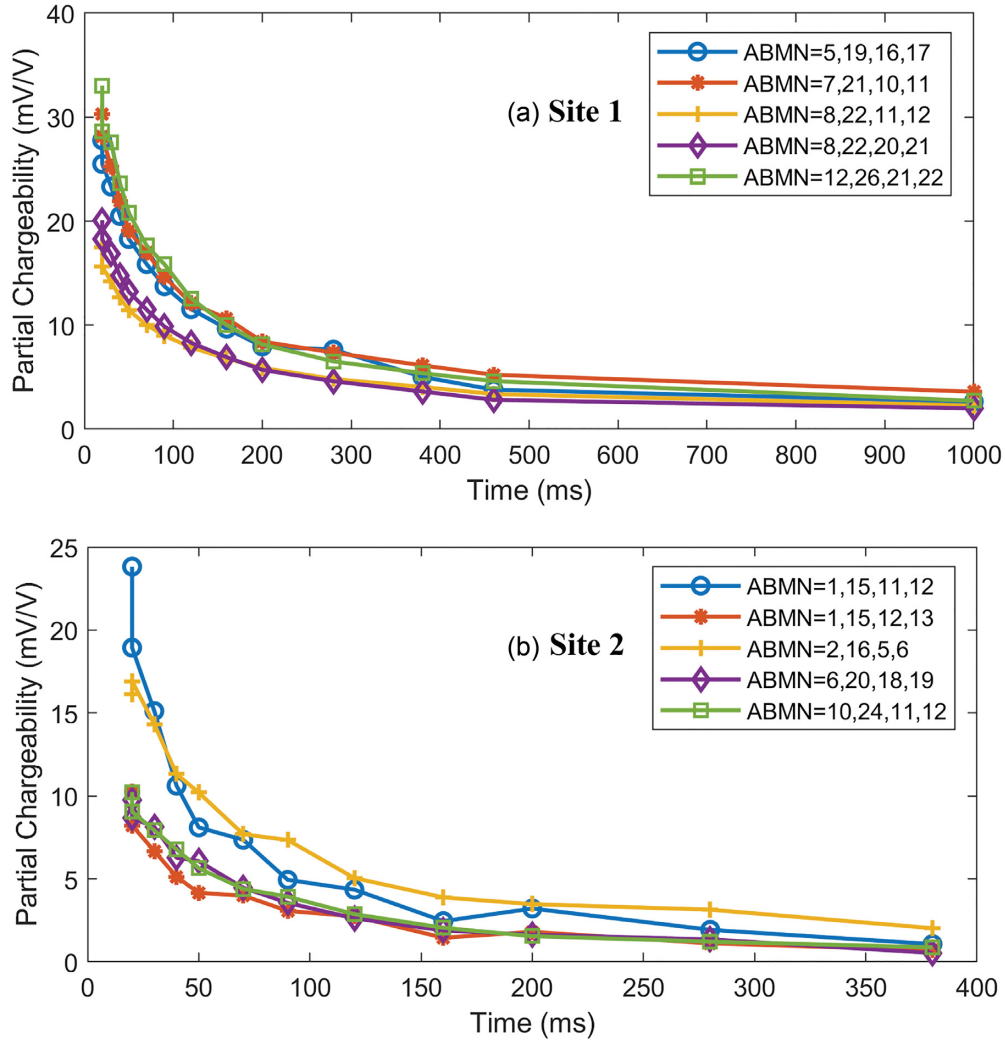
Figure 17. Secondary voltage decay curve recorded in the field. For the inversion, we use only the first window W1 of the data. (a) Examples of decay curves for Site 1. (b) Examples of decay curves for Site 2. A and B denotes the current electrodes and M and N the voltage electrodes. These trends show the high quality of the recorded data set.

provides a good illustration of this approach. The three layers resistor model has three components in parallel, one of which has its elements in series. In this model, the conductivity of the rock σ (S m^{-1}) can be expressed as,

$$\sigma_\infty = \frac{1}{F}\sigma_w + C'\sigma_{ss}^\infty + \frac{\sigma_{ss}^\infty \sigma_w}{A\sigma_{ss}^\infty + B'\sigma_w}, \tag{29}$$

where σ_w (S m^{-1}) denotes the pore water conductivity, F denotes the (intrinsic) formation factor of the porous material (dimensionless), and A, B' and C' (keeping the same notations as in Revil *et al.* 2018a) are three textural parameters. We will show below that A, B' and C' can be derived properly from a very fundamental theory. In eq. (29), the conductivity σ_{ss}^∞ denotes the instantaneous conductivity of the grains and is given by eq. (7). Eq. (29) can be compared to eq. (15) of Lévy *et al.* (2018),

$$\sigma_\infty = \frac{1}{F}\sigma_w + b_2 + \frac{c_2\sigma_w}{1 + (c_2/d_2)\sigma_w}. \tag{30}$$

These equations are strictly identical. A comparison between the two expressions yields

$$b_2 = C'\sigma_{ss}^\infty, \tag{31}$$

$$c_2 = 1/A, \tag{32}$$

$$d_2 = \sigma_{ss}^\infty/B', \tag{33}$$

The approach developed however by Wyllie & Southwick (1954) and Lévy *et al.* (2018) is phenomenological, so no clear meaning could be found in Lévy *et al.* (2018) between the three parameters b_2, c_2 and d_2 and the characteristics of the core samples. The recent modeling approach adopted by Revil *et al.* (2018a) provides, however, a clear physical meaning to these parameters in terms of textural parameters defined for any microstructure. In short, a rigorous physics-based model has been developed in the literature based on volume averaging concepts of the Joule dissipation of energy (Johnson *et al.* 1986; Johnson & Sen 1988; Bernabé & Revil 1995; Revil & Glover 1997). The model developed by Johnson *et al.* (1986) and Johnson & Sen (1988) is based on developing rigorous high and low-salinity asymptotic limits for the instantaneous conductivity and connecting these linear asymptotic limits using a Padé approximant (i.e. a ratio of polynomials, see Johnson *et al.* 1986; Johnson & Sen 1988). The final result can be written as (see details in Johnson *et al.* 1986; Johnson & Sen 1988; Bernabé & Revil 1995;
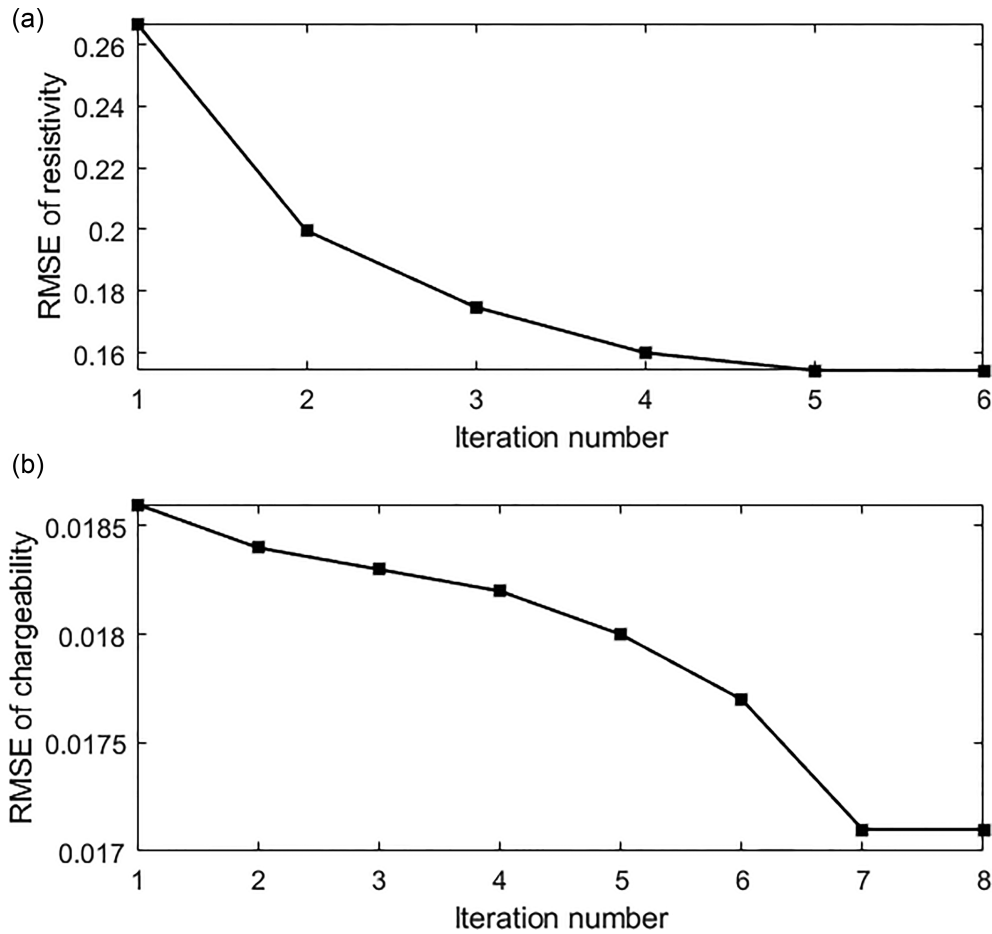
Figure 18. Convergence of the data misfit function for the apparent resistivity and apparent chargeability data for Site 1. Electrical resistivity has converged at the 6th iteration while chargeability has converged at iteration 9. RMSE stands for root mean square error.

Revil *et al.* 2018a)

$$\sigma_\infty = \sigma_w g(x_\infty),\tag{34}$$

$$g(x_\infty) = \frac{b + cx_\infty + dx_\infty^2}{1 + ax_\infty},\tag{35}$$

where $x_\infty = \Sigma_S^\infty/\sigma_w$, Σ_S^∞ (in S) denotes the (instantaneous) specific surface conductivity of the clay minerals. It is defined as the difference between the conductivity in the range of the double layer and that in the bulk solution integrated over the thickness of the double layer (Revil & Glover 1997). It can be related to the CEC and the mobility of the counterions in the Stern and diffuse layers (see details in Revil *et al.* 2018a). For Na^+, $T = 25\,°C$, Σ_S is on the order of 4×10^{-9} S for montmorillonite, CEC = 90 meq/100 g (see Cremers & Laudelout 1965, Cremers *et al.* 1966) and $\Sigma_S \approx 5 \times 10^{-9}$ S in Revil *et al.* 2018a). Eqs (8) and (9) should satisfy the two asymptotic limits,

$$\sigma_\infty = \sigma_w \left[\frac{1}{F} + \frac{2}{\Lambda F} x_\infty + O\left(\frac{2}{\Lambda} x_\infty\right)^2 \right],\tag{36}$$

$$\sigma_\infty = \sigma_w \left[\frac{\lambda}{2f} + \frac{1}{f} x_\infty + O\left(\frac{\lambda}{2} \frac{1}{x_\infty}\right)^2 \right],\tag{37}$$

at high $(2x_\infty/\Lambda = 2\Sigma_S^\infty/\sigma_w\Lambda << 1)$ and low $(2x_\infty/\lambda = 2\Sigma_S^\infty/\sigma_w\lambda >> 1)$ salinities, respectively, and where the Bachmann–Landau notation is again used for the asymptotic developments. High and low salinities are defined with respect to the isoconductivity point. The intrinsic formation factor is defined as $F = [g(0)]^{-1}$. The four parameters entering this fundamental model can be related to the four fundamental textural parameters, which are F (dimensionless), Λ (m), f (m) and λ (m) as,

$$a = \frac{\frac{2}{\Lambda}}{\frac{\lambda F}{2f} - 1},\tag{38}$$

$$c = \frac{\frac{2}{\Lambda}}{F - \frac{2f}{\lambda}},\tag{39}$$

$$b = 1/F,\tag{40}$$

$$d = a/f.\tag{41}$$

The quantity $1/F$ and Λ appear as an effective porosity and the size of the pore throats in the porous material, respectively (see details in Bernabé & Revil 1995; Revil *et al.* 2018a).

Eqs (34) and (35) accurately capture the non-linear behaviour of smectite-rich rocks very well (Figs 13 and 14). Since this model is derived from fundamental physics (i.e. the upscaling of Joule dissipation), it is very general with four well-defined fundamental parameters describing the effect of the texture on the conductivity
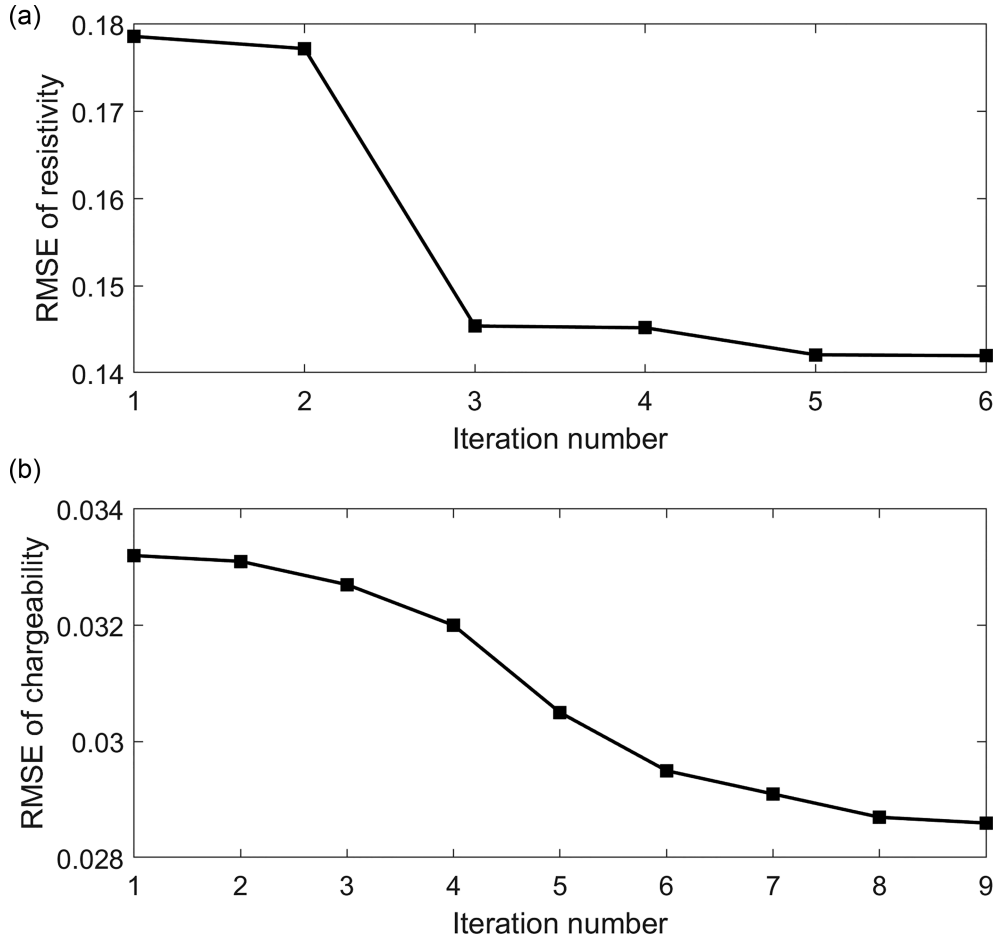
Figure 19. Convergence of the data misfit function for the apparent resistivity and apparent chargeability data for Site 2. Electrical resistivity has converged at the 6th iteration while chargeability has converged at iteration 8. RMSE stands for root mean square error.

curve (see Johnson *et al.* 1986; Johnson & Sen 1988; Bernabé & Revil 1995 for a discussion on the meaning of these parameters). No assumption has to be made regarding the microstructure. Revil *et al.* (2018a) demonstrated the equivalence between the three resistors model and the general Padé approximant model described above. Such equivalence leads to (see Revil *et al.* 2018a, for the mathematical details),

$$A = \frac{1}{\frac{\lambda}{2f} - \frac{1}{F}}, \tag{42}$$

$$B' = \frac{1}{m} \frac{1}{1 - \frac{\Lambda F}{2f}}, \tag{43}$$

$$C' = \frac{m\Lambda F}{2f}, \tag{44}$$

and where m is the porosity (cementation) exponent found in Archie's first law $F = \phi^{-m}$ (Archie 1942). Therefore the parameters in Lévy *et al.* (2018) are related to the most fundamental textural parameters F, Λ, f and λ of a porous material by

$$b_2 = \frac{m\Lambda F}{2f} \sigma_{ss}^\infty, \tag{45}$$

$$c_2 = \frac{\lambda}{2f} - \frac{1}{F}, \tag{46}$$

$$d_2 = m \left(1 - \frac{\Lambda F}{2f} \right) \sigma_{ss}^\infty. \tag{47}$$

The same type of equations (see eqs 34–37) can be written for the dc conductivity σ_0 as a function of the dc conductivity of the grains σ_{ss}^0. In the context of the dynamic Stern layer model, the specific surface conductivity has low and high frequencies asymptotic limits given by
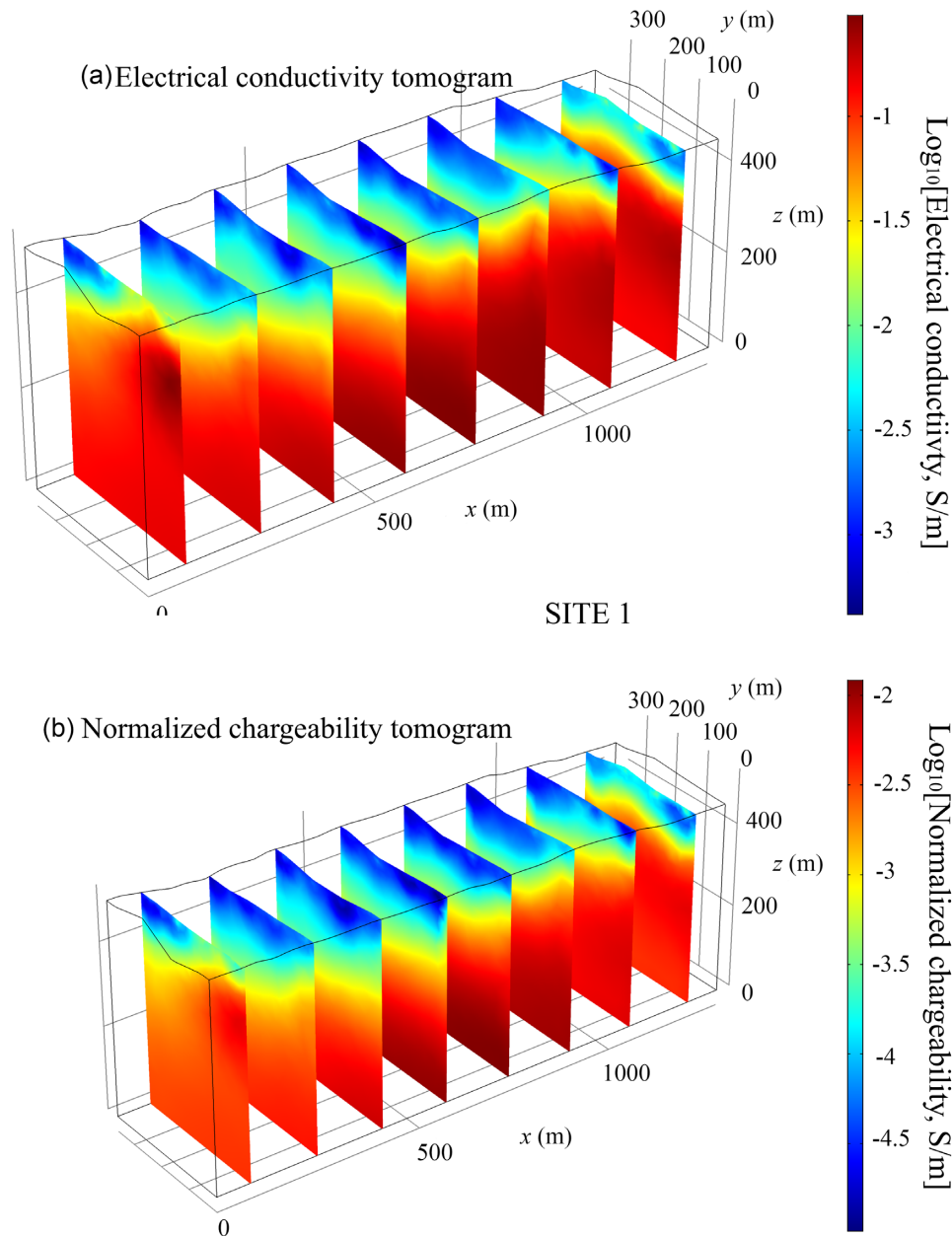
$$\lim_{\omega \to \infty} \Sigma_S* = \Sigma_S^\infty = Q_S B, \tag{48}$$

$$\lim_{\omega \to 0} \Sigma_S* = \Sigma_S^0 = Q_S(B - \lambda), \tag{49}$$

where Σ_S* (in S) described the complex specific surface conductivity of the electrical double layer, ω denotes the angular frequency of the applied electrical field, Q_S (in C m^{-2}) denotes the surface charge density on the mineral surface (Stern and diffuse layers included). With eq. (4), the high salinity (HS) and low salinity (LS) asymptotic limits are given by,

$$M_n^{HS} = \frac{1}{F} \frac{2}{\Lambda} \left(\Sigma_S^\infty - \Sigma_S^0 \right) = \frac{1}{F} \frac{2}{\Lambda} Q_S \lambda, \tag{50}$$

$$M_n^{LS} = \frac{1}{f} \left(\Sigma_S^\infty - \Sigma_S^0 \right) = \frac{1}{f} Q_S \lambda. \tag{51}$$
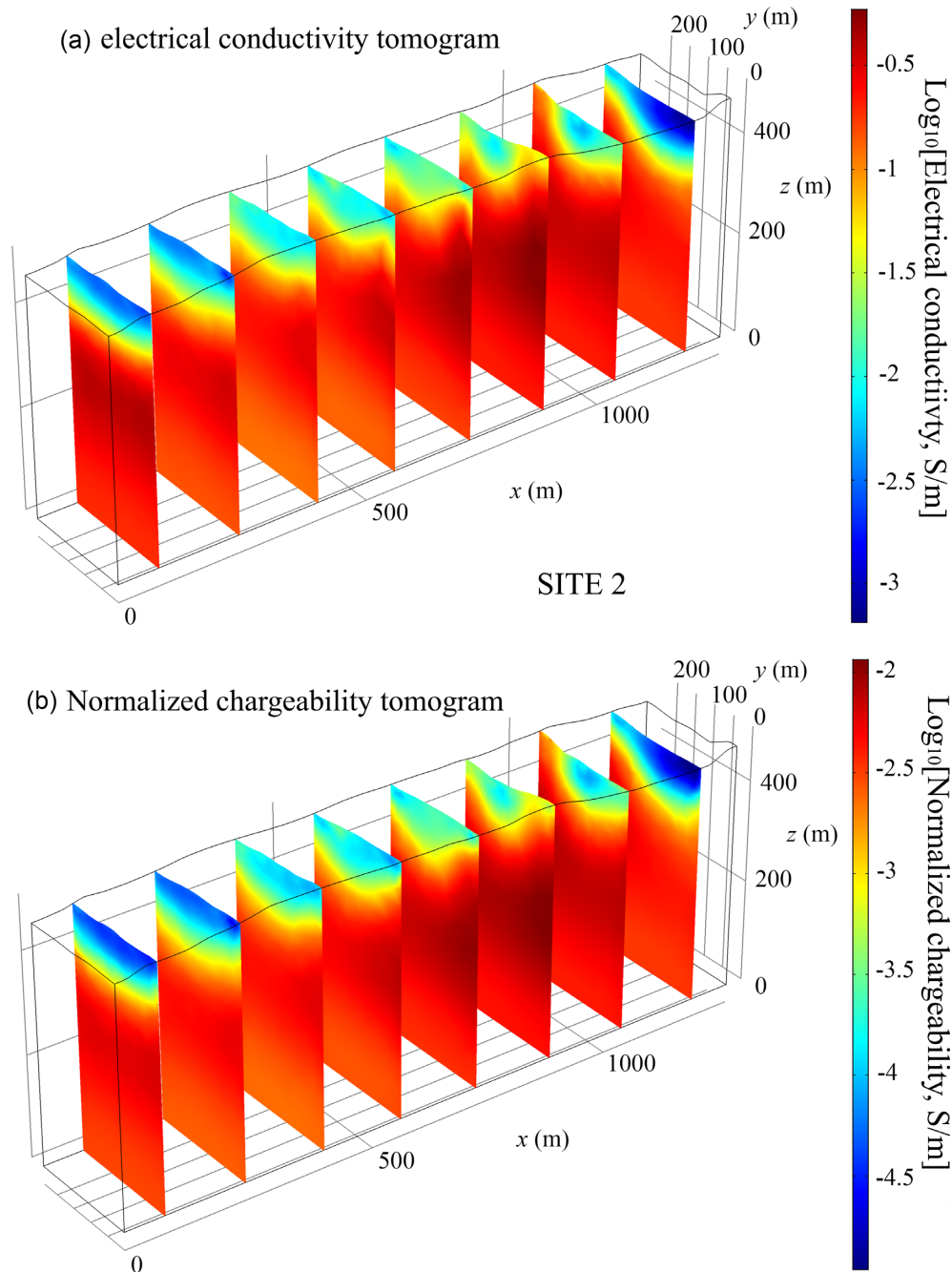
Figure 20. Tomograms at Site 1. (a) 3-D electrical conductivity tomogram (see position in Fig. 15). (b) 3-D normalized chargeability tomogram.

We can now demonstrate that the low salinity asymptotic limit of the normalized chargeability is necessarily smaller than its high salinity asymptotic limit. This is easily proven using the inequality discussed in Revil *et al.* (2018a) for the conductivity model, that is $2/F\Lambda \geq 1/f$ (see also Revil & Glover 1997). It follows that the normalized chargeability is expected to be an increasing function of the pore water conductivity as we found for the DEM. In order to analyse how the normalized conductivity increases with the pore water conductivity, we first look at the Padé approximant. We use the following values for the four textural parameters $\Lambda = 3$ nm, $\lambda = 60$ nm, $F = 10$ and $f = 30$ nm. This yields $A = 1.11$ (dimensionless), $B = 30$ nm and $C = 0.033$ nm^{-1}. We use also from Revil *et al.* (2017a,b), $Q_S = 0.81$ C m^{-2} and we obtain

$\Sigma_S^\infty = Q_S B = 3.34 \times 10^{-9}$ S and $\Sigma_S^0 = Q_S(B - \lambda) = 2.11 \times 10^{-9}$ S and therefore $\Sigma_S^\infty - \Sigma_S^0 = 1.23 \times 10^{-9}$ S. We observe that around the isoconductivity point, the normalized chargeability is an increasing function of the pore water conductivity (Fig. 14).

While the equations developed in this section are more general than the one used in the DEM theory presented in Section 2, the drawback of the volume averaging approach (or equivalently the three resistors model) is to use four textural parameters to capture the non-linear behaviour of the conductivity curve rather than two parameters used in the DEM approach. The reasons for this difference have been explored in details in Revil *et al.* (2018a). Therefore, for practical applications, we prefer to use the DEM approach to interpret field data.

Figure 21. Tomograms at Site 2. (a) 3-D electrical conductivity tomogram of Site 2 (see position in Fig. 15). (b) 3-D normalized chargeability tomogram. The data show a layer characterized by high conductivity and normalized chargeability values at depth corresponding to the clay-cap.

4 FIELD APPLICATION

4.1 Data acquisition

The data used in this section were acquired at the end of the Summer 2017. Two field sites (named 1 and 2 below) were investigated (Fig. 15). The sites were chosen because they are close to wells in which a relatively shallow clay cap was recognized at a depth of few hundred meters (see Árnason *et al.* 2010; Levy *et al.* 2018, for details). Site 1 consists of 4 parallel profiles separated by a distance of 100 m. Each profile (1240 m long) is characterized by a

set of 32 × 2 electrodes (32 electrodes for the current injection and 32 for the voltage measurements) with a separation of 40 m. Site 2 comprises 5 profiles parallel to each other. The profile interval is 50 m and the same electrode configuration than Site 1 is used here too. The data were acquired using time-domain induced polarization measurements (Fig. 16a). For each profile and following the strategy of Dahlin *et al.* (2002), we used two cables parallel to each other and separated by a distance of 5 m. One of these cable comprises the electrodes used to inject the electrical current and the second cable is used for the electrodes measuring the voltage
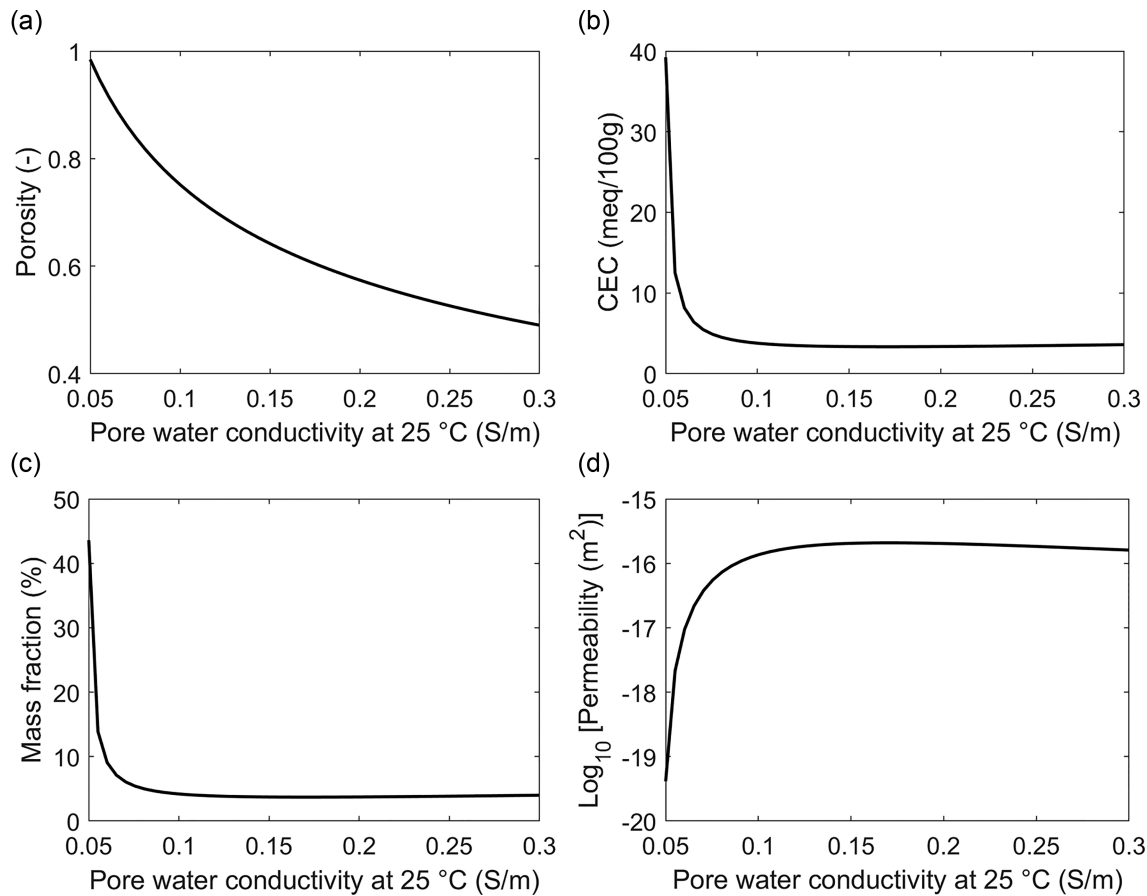
Figure 22. Sensitivity analysis of the petrophysical parameters to the choice of the pore water conductivity for a point of coordinates ($x = 900$, $y = 120$, $z = 240$ m) (inside the clay cap, Site 1). The initial pore water conductivity is chosen in the range 0.05 to 0.3 S m^{-1}. We see that a value of 0.3 S m^{-1} yield a reasonable estimate of the porosity. This value is used to interpret the conductivity and normalized chargeability tomograms. (a) Porosity. (b) Cation exchange capacity. (c) Mass fraction of smectite. (d) Permeability.

differences (Fig. 16b). Such configuration avoids two issues: (1) When the wires in one cable are used for both current injection and voltage measurement, electromagnetic cross-talks interfere with the measurements. (2) An electrode that has been used as current electrode in a high contact resistance environment generates spurious unstable voltages for several minutes after shutting down the primary current. Therefore it cannot be used as a voltage electrode during that time.

The data were acquired with an ABEM SAS4000 with a 4-channels capability and an ABEM LS instrument (8-channels). Multigradient arrays were adopted for the collection of the apparent resistivity and apparent chargeability data. We acquired 920 apparent resistivities and apparent chargeabilities for Site 1. A total of 1179 apparent resistivity and apparent chargeability data were obtained at Site 2. The data sets were inverted with the codes developed in Soueid Ahmed *et al.* (2018), Ghorbani *et al.* (2018) and Qi *et al.* (2018) taking into account the topography. During the modeling, unstructured tetrahedrons were used to discretize the models for their good ability to emulate the topography. 86 460 and 85 074 tetrahedral elements were generated for the core domains in site 1 and 2, respectively. For both sites, the topography is considered during inversion. For site 1, the maximum z-axis is 532 m and the minimum is 451 m, while for site 2 the maximum is 507 m and the minimum is 456 m. The characteristic secondary voltage decay curves (plotted as apparent chargeabilities) indicate the quality of the data (Fig. 17). We consider a dead time of 0.085 s before starting recording the secondary voltages. For the inversion, we use only the first window W1 (see Fig. 16a for its definition) with a duration of 0.025 s. The inversions of the geophysical data converge well as shown in Figs 18 and 19 for Sites 1 and 2, respectively.

The apparent resistivity data are first inverted in terms of a 3-D tomogram of electrical conductivity (Fig. 20). Then, this final 3-D conductivity model is used to invert the apparent chargeability data in order to get a 3-D tomogram of chargeability. The tomogram of chargeability is finally converted to a tomogram of normalized chargeability by multiplying the chargeability tomogram by the conductivity tomogram cell-by-cell. At both sites, a ∼500-m section was imaged (Fig. 20). At the two sites, we observe a shallow layer characterized by a low conductivity (10^{-3} S m^{-1}) and of normalized chargeability (10^{-5} S m^{-1}) (see Figs 21 and 22), with values that are typical of poorly altered volcanic rocks containing smectite (Ghorbani *et al.* 2018). A deeper layer is characterized by a higher conductivity (10^{-1} S m^{-1}) and a higher normalized chargeability (10^{-2} S m^{-1}). These values of the second layer are typical of very altered rocks likely associated with smectite (Ghorbani *et al.* 2018). Actually, we know from XRD analysis on core samples from Wells KH-01 and KH-03 that at these depths, a high proportion of smectite (up to 10–20 weight per cent) is present in the volcanic rocks (Lévy *et al.* 2018).
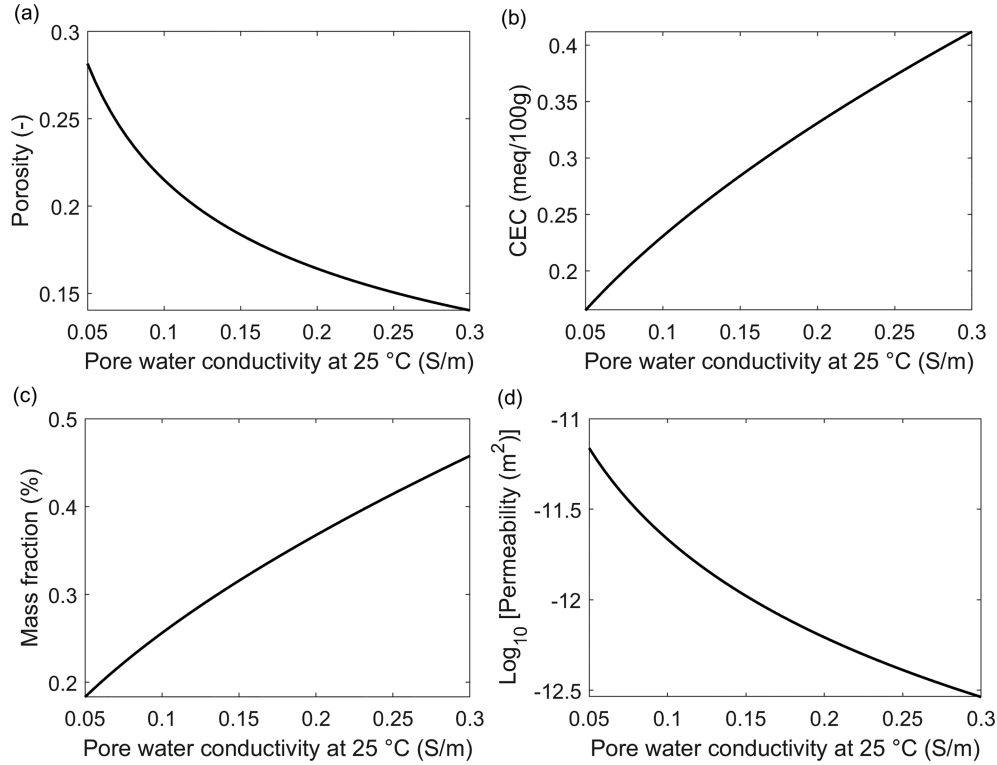
Figure 23. Sensitivity analysis of the petrophysical parameters to the choice of the pore water conductivity for a point of coordinates (coordinates $x = 1200$ m, $y = 120$ m, $z = 20$ m, that is just above the clay cap in the unaltered portion of the investigated domain, Site 2). The initial pore water conductivity is chosen in the range 0.05–0.3 S m^{-1}. (a) Porosity. (b) Cation exchange capacity. (c) Mass fraction of smectite. (d) Permeability.

4.2 Petrophysical modeling approach

We can now use the tomograms of conductivity and normalized chargeability to image the porosity, CEC, smectite content, and permeability of the clay cap. In order to derive the porosity and the CEC tomograms, we assume that the porous material is fully water-saturated since the clay cap is very shallow (few hundreds meters). Starting with eqs (12) and (24), we have

$$\sigma_\infty \approx \frac{1}{F}(\sigma_w + m\,B\,Q_V),\tag{52}$$

$$M_n^{HS} \approx m\,\frac{1}{F}\lambda Q_V.\tag{53}$$

Combining these two equations and using $\lambda = BR$ ($R = 0.10$), we obtain the following relationship between the surface conductivity and the normalized chargeability:

$$\frac{m}{F}B Q_V = \frac{M_n^{HS}}{R}.\tag{54}$$

Therefore the conductivity and the normalized chargeability can be related to each other by

$$\sigma_\infty \approx \frac{\sigma_w}{F} + \frac{M_n^{HS}}{R}.\tag{55}$$

Finally combining eq. (55) with Archie's law $F = \phi^{-m}$, the porosity can be obtained by using the following equation

$$\phi = \left(\frac{\sigma_\infty - M_n^{HS}/R}{\sigma_w(T)}\right)^{1/m},\tag{56}$$

with $m = 2.57$ as an average value (see Fig. 8), $R = 0.10$ (independent of temperature) and σ_∞ and M_n^{HS} denote the measured

conductivity and normalized chargeability distributions. The pore water conductivity $\sigma_w(T)$ depends on temperature according to eq. (19) in which we need the value of the pore water conductivity $\sigma_w(T_0)$ at the reference temperature $T_0 = 25\,°C$ (298 K). As a side note, T_0 is the reference temperature and not the ground surface temperature defined below as T_S. From Stefánsson (2014), we have a pore water conductivity $\sigma_w(T_0 = 25\,°C = 470\ \mu S\ cm^{-1}$ (0.05 S m^{-1}). According to Árnason *et al.* (2010), the pore water conductivity value is in the range $\sigma_w(T_0 = 25\,°C) = 0.15$–0.30 S m^{-1}. Flóvenz *et al.* (2005) used $\sigma_w(T_0 = 25\,°C) = 780\ \mu S\ cm^{-1}$ (0.08 S m^{-1}). Finally, Lévy *et al.* (2018) used $\sigma_w(T_0 = 25\,°C) = 0.03$–0.10 S m^{-1}.

Once the porosity has been determined, we need to compute the CEC distribution. From eq. (53), we obtain the following expression for the CEC

$$\text{CEC} = \frac{M_n^{HS}}{m\,\phi^m\,\rho_g\lambda(T)}\left(\frac{\phi}{1-\phi}\right),\tag{57}$$

where we use $\rho_g = 2900$ kg m^{-3} (as an average value for the volcanic rocks in Ghorbani *et al.* 2018), $m = 2.57$ (Fig. 8), $\lambda(T)$ is given by eq. (21) with $\lambda(\text{Na}^+, 25\,°C) = 3.0 \pm 0.7 \times 10^{-10}$ m^{-2}s^{-1}V^{-1}, and M_n^{HS} denotes the measured normalized chargeability distribution. The CEC is given in C kg^{-1} (1 meq/100 g = 963.20 C kg^{-1}). The quantities σ_∞^b and M_n^b are measured at the *in situ* temperature, so they do not need to be corrected for the effect of the temperature. We need to know the temperature as a function of depth in order to compute $\lambda(T)$ from eq. (21). In the upper part of the investigated system, the temperature is taken from the equilibrium temperature as,

$$T(z) = T_S + G\,z,\tag{58}$$

(a)

(b)
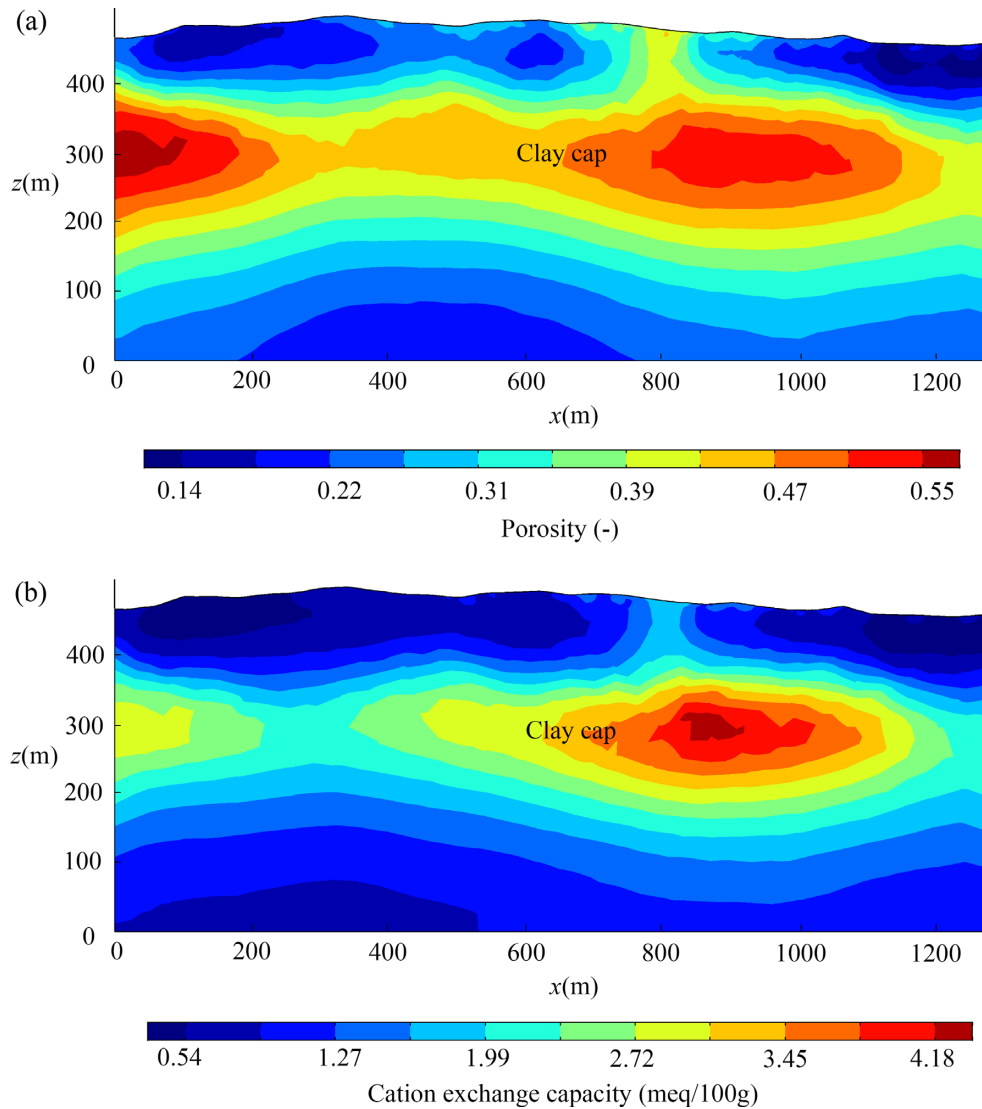
Figure 24. Porosity and CEC showing the clay cap (Site 2). The inversion is successful in underlying the clay-cap and its properties.

where z denotes the depth below the ground surface, T_S denotes the ground surface temperature at the two sites ($10\,°C$) and with G defining the geothermal gradient ($G = 600\,°C\,km^{-1}$).

Once the porosity and the CEC have been determined, the other parameters of interest can be computed. From eq. (9), neglecting the background residual CEC due to other minerals, the mass fraction of smectite can be obtained as,

$$\varphi_W(S) \approx \frac{CEC}{CEC(S)}, \tag{59}$$

where $CEC(S) = 90$ meq/100 g and denotes the CEC of smectite (Fig. 4b). Finally, the permeability can be computed either from eq. (27) or eq. (28). In this section, we will use eq. (28) because it provides a good permeability prediction.

4.3 Results and interpretation

As explained above, we first start with a sensitivity analysis regarding the pore water conductivity taken in the range $\sigma_w(T_0 = 25°C) = 0.05$ to 0.3 S m^{-1} at Krafla volcano. We select two points in the investigated 3-D volume at Site 2, one being in the clay cap

(coordinates $x = 900$ m, $y = 120$ m, $z = 240$ m) and the second closer to the ground surface in what is supposed to be a relatively unaltered area (coordinates $x = 1200$ m, $y = 120$ m, $z = 20$ m). Reasonable estimates for the porosity (expected range 0.30–0.50) and CEC (expected range 2–20 meq/100 g) are only obtained with a pore water conductivity of $\sigma_w(T_0 = 25°C) \approx 0.30 \pm 0.05$ S m^{-1} for Site 2, consistent with the range discussed above (see Figs 23 and 24).

Then, with this pore water conductivity value, we use the relationships discussed in Section 4.2 to compute the 3-D tomograms of porosity, CEC, smectite content and permeability (Figs 24 and 25 for Site 2). A vertical cross-section distributions of these properties (profile at $y = 120$ m) is displayed in Figs 26 and 27. The clay cap is characterized by high porosity (in the range 0.40–0.50), high CEC values (3–5 meq/100 g), and therefore high smectite content (few per cents), and low permeability (0.1–1 milliDarcy). The clay cap is rather flat in this area. The perched aquifer above the clay cap is characterized by higher resistivities, lower porosities and CEC values. The more resistive formations located deeper than the clay cap appear to have a smaller clay content.
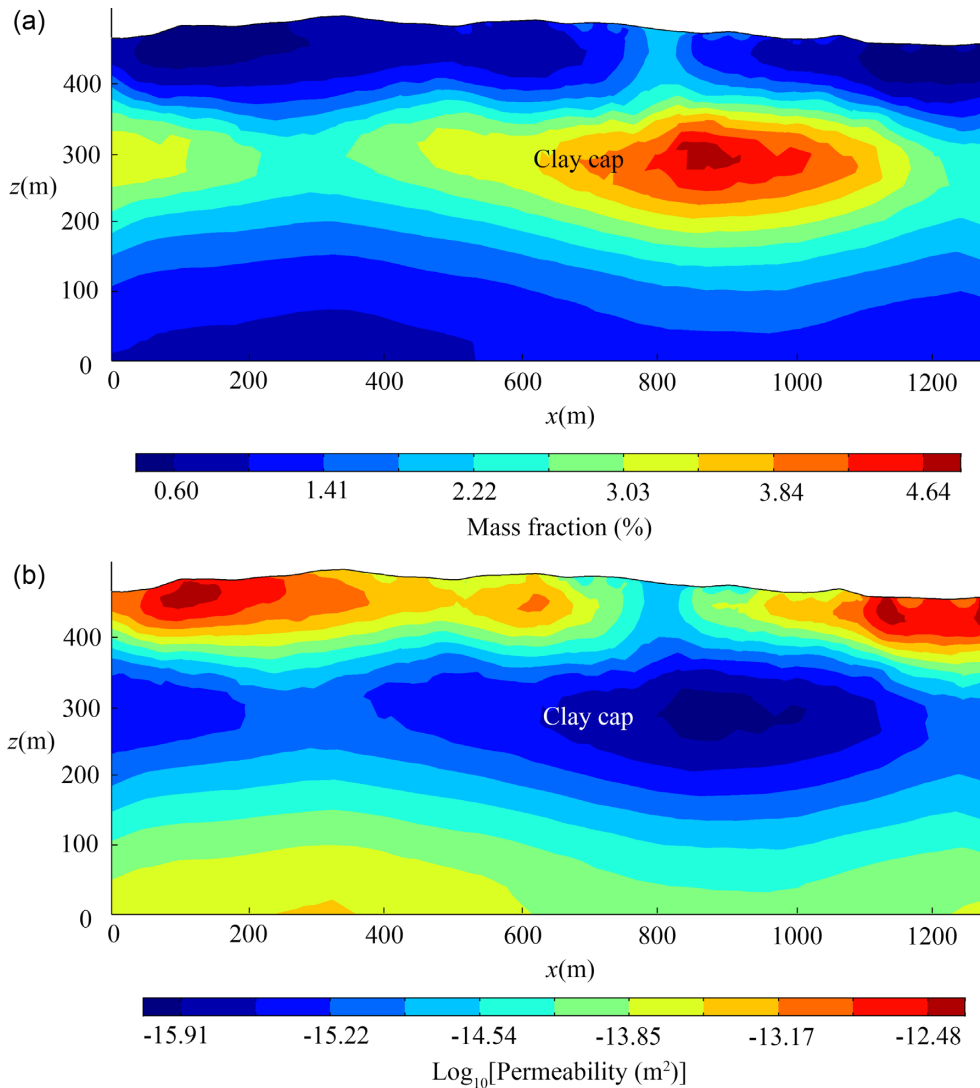
Figure 25. The high smectite content and low permeability underline the clay cap (Site 2). The clay cap is characterized by low permeability in the range 0.1–1 mD (10^{-14}–10^{-16} m^2). The inversion is successful in underlying the clay-cap and its properties.

The same work is done at Site 1. We obtain a pore water conductivity of 0.05 ± 0.02 S m^{-1} in order to get reasonable values of porosity and CEC (as discussed above for Site 2) so substantially smaller than at Site 2. A 2-D cross-section showing the distributions of the porosity, CEC, smectite content and permeability are shown in Figs 26 and 27. The values we have obtained are in agreement with the borehole data exhibited in Lévy *et al.* (2018, their fig. 12). This seems to indicate that we are successful with our approach in imaging the porosity and CEC of volcanic rock formations.

5 CONCLUSIONS

We have developed a complete consistent theory of conductivity and chargeability in smectite-rich volcanic rocks using the DEM theory and this theory simplifies to the now well-established equations for low CEC materials. The following conclusions have been reached.

(i) The new model captures the non-linear behaviour between the rock conductivity and the pore water conductivity for smectite rich volcanic rocks. An alternative approach based on the volume averaging theory (which is shown to be equivalent to the three-resistor model) requires four textural parameters to accomplish the same task. The DEM theory is therefore more practical to use in interpreting field data.

(ii) The new model agrees with the dependence of the grain conductivity with the excess charge per unit pore volume, which depends in turn on the measured CEC (obtained independently with titration experiments using for example the cobalt hexamine method) and the (connected) porosity. The slope of the linear trend provides the value of the effective mobility of the counterions for surface conduction including in the interlayer pore space.

(iii) The new model agrees with the dependence of the normalized chargeability with the excess charge per unit pore volume. The slope of the linear trend provides the value of the effective mobility of the counterions for surface polarization including in the interlayer pore space.

(iv) The new model can be applied to time-domain induced polarization data in the field in order to provide tomograms of porosity, CEC, smectite content, and permeability with application to the detection of smectite-rich clay caps of geothermal systems. The permeability can be derived from the porosity and the CEC. An
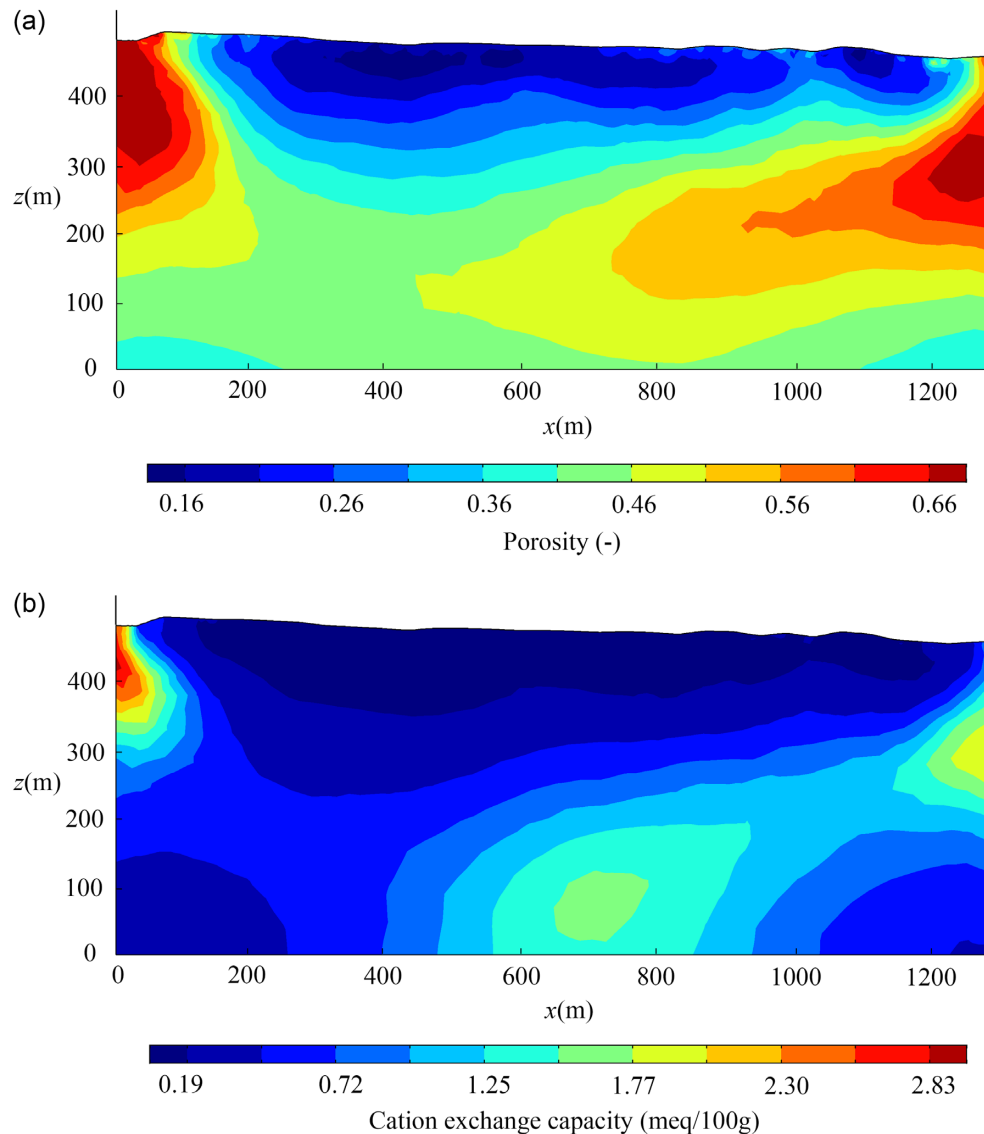
Figure 26. Porosity (dimensionless) and CEC (in meq/100 g) for a cross-section at Site 1. We can observe also the clay cap but its structure is more complicated than at Site 2. The inversion is successful in underlying the clay-cap and its properties.
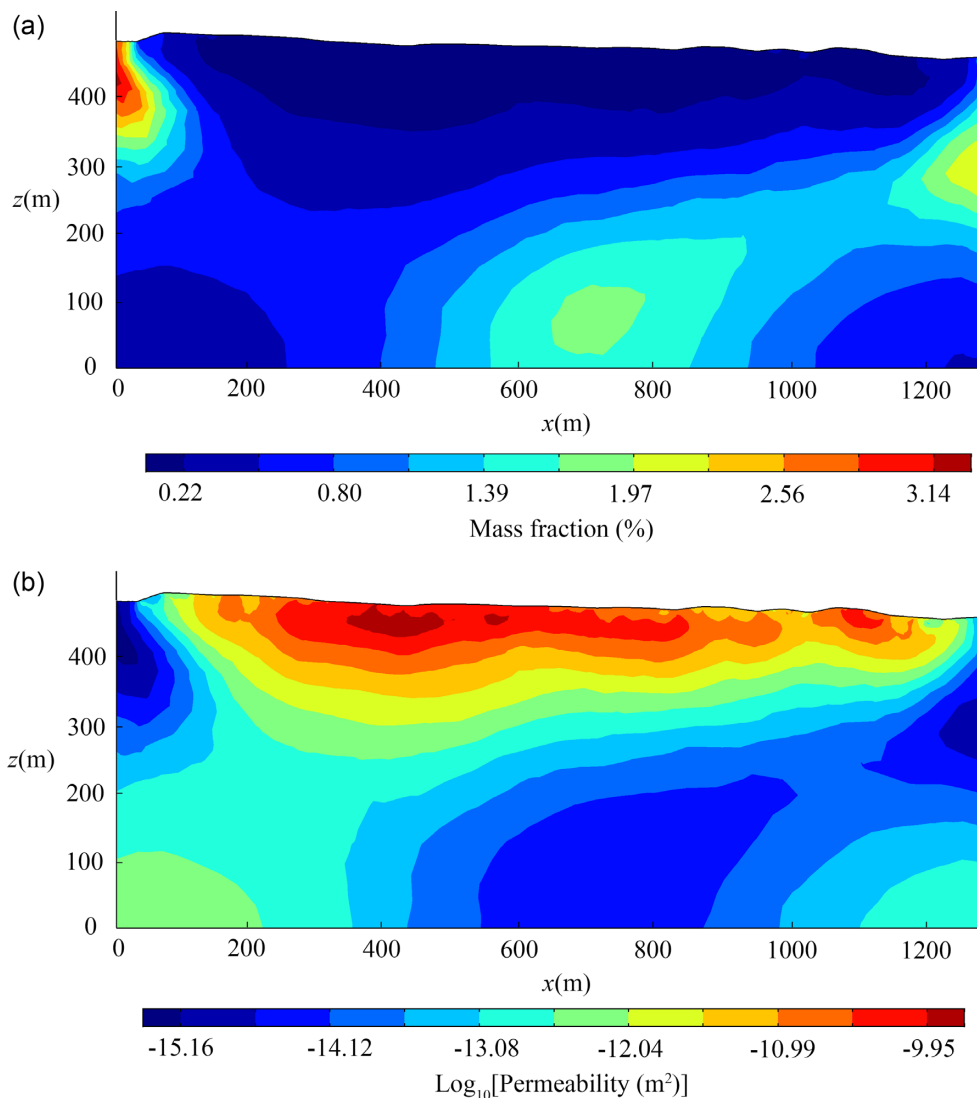
application to a clay cap in Krafla in Iceland indicates a porosity of 40–50 per cent, a CEC in the range 3–5 meq/100 g (3–5 per cent weight per cent smectite), and a permeability in the range 0.1–1 mD.

While the present study was restricted to a depth of ∼500 m, recent technological developments such as the FullWaver equipment from IRIS can be used to image induced polarization properties to depths of few kilometers. We have now the ability to image induced polarization properties of volcanoes in 3-D or 4-D. 4-D induced polarization tomography of active volcanoes will be the subject of a future contribution.

Figure 27. Smectite content (mass fraction) and permeability (in m^2) for a cross-section at Site 1. The permeability of the clay cap is also on the order of the milliDarcy.

REFERENCES

Aizawa, K., Ogawa, Y. & Ishido, T., 2009. Groundwater flow and hydrothermal systems within volcanic edifices: delineation by electric self-potential and magnetotellurics, *J. geophys. Res.,* **114,** B01208, doi:10.1029/2008JB005910.

Archie, G.E., 1942. The electrical resistivity log as an aid in determining some reservoir characteristics, *Trans. AIME,* **146,** 54–62.

Árnason, K., Már Vilhjálmsson, A. & Björnsdóttir, T., 2010. A study of the Krafla vocano using gravity micro-earthquake and MT data, in *Presented at Short Course V on Exploration for Geothermal Resources,* organized by UNU-GTP, GDC and KenGen, at Lake Bogoria and Lake Naivasha, Kenya, Oct. 29–Nov. 19, 2010.

Bernabé, Y. & Revil, A., 1995. Pore-scale heterogeneity, energy dissipation and the transport properties of rocks, *Geophys. Res. Lett.,* **22**(12), 1529–1552.

Bibby, H.M., Caldwell, T.G., Davey, F.J. & Webb, T.H., 1995. Geophysical evidence on the structure of the Taupo Volcanic Zone and its hydrothermal circulation, *J. Volc. Geotherm. Res.,* **68,** 29–58.

Bibby, H.M., Risk, G.F., Caldwell, T.G. & Bennie, S.L., 2005. Misinterpretation of electrical resistivity data in geothermal prospecting: a case study from the Taupo Volcanic Zone, in *Proceedings of the World Geothermal Congress,* Antalya, Turkey.

Binley, A., Hubbard, S.S., Huisman, J.A., Revil, A., Robinson, D.A., Singha, K. & Slater, L.D., 2015. The emergence of hydrogeophysics for improved understanding of subsurface processes over multiple scales, *Water Resour. Res.,* **51,** 3837–3866.

Browne, P.R.L., 1978. Hydrothermal alteration in active geothermal fields, *Ann. Rev. Earth planet. Sci.,* **6,** 229–250.

Bruggeman, D.A.G., 1935. Physikalischer konstanten von heterogenen Substanzen, *Ann. Phys.-Berlin,* **24,** 636–664.

Bussian, A.E., 1983. Electrical conductance in a porous medium, *Geophysics,* **48**(9), 1258–1268.

Colten-Bradley, V.A., 1987. Role of pressure in smectite-dehydration – effects on geopressure and smectite-to-illite transformation, *AAPG Bull.,* **71**, 1414–1427.

Cosenza, P., Ghorbani, A., Camerlynck, C., Rejiba, F., Guérin, R. & Tabbagh, A., 2009. Effective medium theories for modelling the relationships between electromagnetic properties and hydrological variables: a review, *Near Surf. Geophys.,* **7**, 563–578.

Cremers, A. & Laudelout, H., 1965. On the "isoconductivity value" of clay gels, *Soil Sci.,* **100**, 298–299.

Cremers, A.E. & Laudelout, H., 1966. Surface mobilities of cations in clays, *Proc. Soil Sci. Soc. Am.,* **30**, 570–576.

Cremers, A., Van Loon, J. & Laudelout, H., 1966. Geometry effects for specific electrical conductance in cays and soils, *Clays Clay Miner.,* **14**, 149–162.

Cumming, W., 2009. Geothermal resource conceptual models using surface exploration data, in *Proceedings of the Thirty-Fourth Workshop on Geothermal Reservoir Engineering Stanford University,* pp. 7, Stanford, California, February 9–11, 2009, SGP-TR-187.

Cumming, W. & Mackie, R., 2009. MT survey for resource assessment and environmental mitigation at the Glass Mountain KGRA, California Energy Commission, GRDA Report, Geothermal Resources Development Account.

Dahlin, T., Leroux, V. & Nissen, J., 2002. Measuring techniques in induced polarisation imaging, *J. appl. Geophys.,* **50**, 279–298.

de Kronig, R.L., 1926. On the theory of dispersion of X-rays, *J. Opt. Soc. Am. Rev. Sci. Instrum.,* **12**, 547–557.

de Kronig, R.L., 1942. Algemeene theorie der diëlectrische en magnetische verliezen (General theory of dielectric and magnetic losses), *Ned. Tijdschr. Natuurkd.,* **9**, 402–409.

Flóvenz, O.G., Spangenberg, E., Kulenkampff, J., Árnason, K., Karlsdóttir, R. & Huenges, E., 2005. The role of electrical interface conduction in geothermal exploration, in *Proceedings of the World Geothermal Congress 2005,* Antalya, Turkey, 24–29 April 2005.

Fripiat, J.J., Jali, A., Poncelet, G. & André, J., 1965. Thermodynamic properties of adsorbed water molecules and electrical conduction in montmorillonites and silicates, *J. Phys. Chem.,* **69**, 2185–2197.

Friedman, S.P., 2005. Soil properties influencing apparent electrical conductivity: a review, *Comput. Electr. Agric.,* **46**, 45–70.

Gast, R.G., 1966. Applicability of models to predict rates of cation movement in clays, *Soil Sci. Soc. Am. Proc.,* **30**, 4–52.

Ghorbani, A., Revil, A., Coperey, A., Soueid Ahmed, A., Roque, S., Heap, M.J., Grandis, H. & Viveiros, F., 2018. Complex conductivity of volcanic rocks and the geophysical mapping of alteration in volcanoes, *J. Volc. Geotherm. Res.,* **357**, 106–127.

Goode, P.A. & Sen, P.N., 1988. Charge density and permeability in clay-bearing sandstones, *Geophysics,* **53**, 610–612.

Gunderson, R., Cumming, W., Astra, D. & Harvey, C., 2000. Analysis of smectite clays in geothermal drill cuttings by the methylene blue method for well site geothermometry and resistivity sounding-correlation, in *Proceedings of the World Geothermal Congress 2000 Kyushu,* pp. 1175–1181, Tohoku, Japan, May 28–June 10, 2000.

Hanai, T., 1960a. Theory of the dielectric dispersion due to the interfacial polarization and its application to emulsions, *Kolloid Z.,* **171**, 23–31.

Hanai, T., 1960b. A remark on the "Theory of the dielectric dispersion due to the interfacial polarization", *Kolloid Z.,* **175**, 61–62.

He, L., Chen, L., Dorji, Xi, X., Zhao, X., Chen, R. & Yao, H., 2016. Mapping the geothermal system using AMT and MT in the Mapamyum (QP) field, lake Manasarovar, Southwestern Tibet, *Energies,* **9**, 855.

Heap, M.J., Kennedy, B.M., Farquharson, J.I., Ashworth, J., Mayer, K., Letham-Brake, M. & Siratovich, P., 2017. A multidisciplinary approach to quantify the permeability of the Whakaari/White Island volcanic hydrothermal system (Taupo Volcanic Zone, New Zealand), *J. Volc. Geotherm. Res.,* **332**, 88–108.

Horpibulsuk, S., Yangsukkaseam, N., Chinkulkijniwat, A. & Du, Y.J., 2011. Compressibility and permeability of Bangkok clay compared with kaolinite, and bentonite, *Appl. Clay Sci.,* **52**, 150–159.

Howard, J.J., 1992. Influence of authigenic clay minerals on permeability, in *Origin, Diagenesis, and Petrophysics of Clay Minerals in Sandstones,* Vol. **47**, SEM Special Publication, doi:10.2110/pec.92.47.0257.

Jennings, S. & Thompson, G.R., 1986. Diagenesis of PlioPleistocene sediments of the Colorado River Delta, southern California, *J. Sediment. Petrol.,* **56**, 89–98.

Johnson, D.L., Plona, T.J. & Kojima, H., 1986. Probing porous media with 1st sound, 2nd sound, 4th sound and 3rd sound, in *Physics and Chemistry of Porous Media,* Vol. **2**, pp. 243–277, eds Jayanth, R. Banavar, J. & Winkler, K.W., Am. Inst. of Phys., Conf. Proc. No 154, New York.

Johnson, D.L. & Sen, P.N., 1988. Dependence of the conductivity of a porous medium on electrolytic conductivity, *Phys. Rev. B,* **37**, 3502–3510.

Jónasson, K., 1994. Rhyolite volcanism in the Krafla central volcano, northeast Iceland, *Bull. Volcanol.,* **56**, 516–528.

Jorgensen, P. & Low, P.F., 1970. Conductance studies of N~montmorillonite water systems, *Israel J. Chem.,* **8**, 325–333.

Kramers, H.A., 1927. La diffusion de la lumière par les atomes, in *Atti del Congresso Internazionale dei Fisici,* Vol. **2**, pp. 545–557, ed. Zanichelli, N., Como-Pavia-Roma, Bologna.

Leroy, P. & Revil, A., 2009. A mechanistic model for the spectral induced polarization of clay materials, *J. geophys. Res.,* **114**, B10202, doi:10.1029/2008JB006114.

Leroy, P., Weigand, M., Mériguet, G., Zimmermann, E., Tournassat, C., Fagerlund, F., Kemna, A. & Huisman, J.A., 2017. Spectral induced polarization of Na-montmorillonite dispersions, *J. Colloid Interf. Sci.,* **505**, 1093–1110.

Lévy, L., Gibert, B., Sigmundsson, F., Flóvenz, Ó.G., Hersir, G.P., Briole, P. & Pezard, P.A., 2018. The role of smectites in the electrical conductivity of active hydrothermal systems: electrical properties of core samples from Krafla volcano, Iceland, *Geophys. J. Int.,* **215**, 1558–1582.

Lima, O.A.L. & Sharma, M.M., 1990. A grain conductivity approach to shaly sandstones, *Geophysics,* **55**, 1347–1356.

Lima, A.T., Loch, J.P.G. & Kleingeld, P.J., 2010. Bentonite electrical conductivity: a model based on series parallel transport, *J. Appl. Electrochem.,* **40**, 1061–1068.

Lockhart, N.C., 1980. Electrical-Properties and the surface characteristics and structure of clays. 1. Swelling clays, *J. Colloid Interf. Sci.,* **74**(2), 509–519.

Meju, M.A., 2002. Geoelectromagnetic exploration for natural resources: models, case studies and challenges, *Surv. Geophys.,* **23**, 133–205.

Mesri, G. & Olson, R.E., 1971. Mechanisms controlling the permeability of clays, *Clays Clay Miner.,* **19**, 151–158.

Meunier, A., 2005. *Clays,* pp. 492, Springer-Verlag.

Mitchell, J.K., 1993. *Fundamentals of Soil Behavior,* Wiley.

Mortensen, A.K. *et al.,* 2009. Krafla Geothermal System. A compilation of explorations and developments of the geothermal system and a reevaluation of the conceptual model, Landsvirkjun Report LV-2009/111 and ÍSOR, ÍSOR-2009/057, Reykjavik, Iceland, pp 180 (in Icelandic).

Muñoz, G., Bauer, K., Moeck, I., Schulze, A. & Ritter, O., 2010. Exploring the Groß Schönebeck (Germany) geothermal site using a statistical joint interpretation of magnetotelluric and seismic tomography models, *Geothermics,* **39**, 35–45.

Muñoz, G., 2014. Exploring for geothermal resources with electromagnetic methods, *Surv. Geophys.,* **35**(1), 101–122.

Niu, Q. & Revil, A., 2016. Connecting complex conductivity spectra to mercury porosimetry of sedimentary rocks, *Geophysics,* **81**(1), E17–E32.

Niu, Q., Revil, A. & Saidian, M., 2016. Salinity dependence of the complex surface conductivity of the Portland sandstone, *Geophysics,* **81**(2), D125–D140.

Olhoeft, G.R., 1985. Low-frequency electrical properties, *Geophysics,* **50**, 2492–2503.

Peacor, D.R., 1989. Variability and temperature of the smectite/illite reaction on gulf coast sediments, *Clay Mineral.,* **24**, 171–180

Pellerin, A., Johnston, M. & Hohmann, W., 1996. A numerical evaluation of electromagnetic methods in geothermal exploration, *Geophysics,* **61**, 121–130.

Qi, Y., Soueid Ahmed, A., Revil, A., Ghorbani, A., Abdulsamad, F., Florsch, N. & Bonnenfant, J., 2018. Induced polarization response of porous media

with metallic particles—Part 7: detection and quantification of buried slag heaps, *Geophysics,* **83,** E277–E291.

Revil, A., 1999. Ionic diffusivity, electrical conductivity, membrane and thermoelectric potentials in colloids and granular porous media: a unified model, *J. Colloid Interf. Sci.,* **212,** 503–522.

Revil, A., 2000. Thermal conductivity of unconsolidated sediments with geophysical applications, *J. geophys. Res.,* **105,** 16 749–16 768.

Revil, A. & Florsch, N., 2010. Determination of permeability from spectral induced polarization data in granular media, *Geophys. J. Int.,* **181,** 1480–1498.

Revil, A. & Glover, P.W.J., 1997. Theory of ionic surface electrical conduction in porous media, *Phys. Rev. B,* **55**(3), 1757–1773.

Revil, A., Cathles, L.M., Losh, S. & Nunn, J.A., 1998. Electrical conductivity in shaly sands with geophysical applications, *J. geophys. Res.,* **103**(B10), 23 925–23 936.

Revil, A., Grauls, D. & Brévart, O., 2002, Bulk mechanical compaction of sand shale mixtures, *J. geophys. Res.,* **107**(B11), 2293.

Revil, A. *et al.*, 2011. Hydrogeology of stromboli volcano, Aeolian Islands (Italy) from the interpretation of resistivity tomograms, self-potential, soil temperature, and soil CO_2 concentration measurements, *Geophys. J. Int.,* **186,** 1078–1094.

Revil, A., Le Breton, M., Niu, Q., Wallin, E., Haskins, E. & Thomas, D.M., 2017a. Induced polarization of volcanic rocks. 1. Surface versus quadrature conductivity, *Geophys. J. Int.,* **208,** 826–844.

Revil, A., Le Breton, M., Niu, Q., Wallin, E., Haskins, E. & Thomas, D.M., 2017b. Induced polarization of volcanic rocks. 2. Influence of pore size and permeability, *Geophys. J. Int.,* **208,** 814–825.

Revil, A. *et al.*, 2017c. Complex conductivity of soils, *Water Resour. Res.,* **53,** doi:10.1002/2017WR020655.

Revil, A., Murugesu, M., Prasad, M. & Le Breton, M., 2017d. Alteration of volcanic rocks: a new non-intrusive indicator based on induced polarization measurements, *J. Volc. Geotherm. Res.,* **341,** 351–362.

Revil, A., Soueid Ahmed, A. & Matthai, S., 2018a. Transport of water and ions in partially water-saturated porous media. Part 3. Electrical conductivity, *Adv. Water Resour.,* **121,** 97–111.

Revil, A., Ghorbani, A., Gailler, L.S., Gresse, M., Panwar, N. & Sharma, R., 2018b. Electrical conductivity and induced polarization investigations at Kilauea volcano, Hawai'i, *J. Volc. Geotherm. Res.,* **368,** 31–50.

Rhoades, J.D., Manteghi, N.A., Shouse, P.J. & Alves, W.J., 1989. Soil electrical conductivity and soil salinity: new formulations and calibrations, *Soil Sci. Soc. Am. J.,* **53,** 433–439.

Sauer, M.C., Southwick, P.F., Jr., Spiegler, K.S. & Wyllie, M.R.J., 1955. Electrical conductance of porous plugs, *Ind. Eng. Chem.,* **47,** 2187–2193.

Sen, P.N., Scala, C. & Cohen, M.H., 1981. A self-similar model for sedimentary rocks with application to the dielectric constant of fused glass beads, *Geophysics,* **46,** 781–795.

Sen, P.N., Straley, C., Kenyon, W.E. & Whittingham, M.S., 1990. Surface-to-volume ratio, charge density, nuclear magnetic relaxation, and permeability in clay-bearing sandstones, *Geophysics,* **55**(1), 61–69.

Shainberg, I. & Levy, R., 1975. Electrical conductivity of Na-Montmorillonite suspensions, *Clays Clay Miner.,* **23,** 205–210.

Shainberg, I., Rhoades, J.D. & Prather, R.J., 1980. Effect of ESP, cation exchange capacity, and soil solution concentration on soil electrical conductivity, *Soil Sci. Soc. Am. J.,* **44,** 469–473.

Slater, L.D. & Glaser, D.R., 2003. Controls on induced polarization in sandy unconsolidated sediments and application to aquifer characterization, *Geophysics,* **68**(5), 1547–1558.

Soueid Ahmed, A. *et al.*, 2018. 3D electrical conductivity tomography of volcanoes, *J. Volc. Geotherm. Res.,* **356,** 243–263.

Spiegler, K.S., Yoest, R.L. & Wyllie, M.R., 1956. Electric potential across porous plugs and membranes: ion exchange resin-solution systems, *Disc. Faraday Soc.,* **21,** 174–185.

Spichak, V. & Manzella, A., 2009. Electromagnetic sounding of geothermal zones, *J. appl Geophys.,* **68,** 459–478.

Stefánsson, A., 2014. *Geochemical Assessment of the Utilization of IDDP#1,* pp. 66, Krafla.

van Olphen, H., 1957. Surface conductance of various ion forms of bentonite in water and the electrical double layer, *J. Phys. Chem,* **61,** 1276–1280.

van Olphen, H. & Waxman, M.H., 1958. Surface conductance of sodium bentonite in water, *Clays Clay Miner.,* **5**(1), 61–80.

Vinegar, H.J. & Waxman, M.H., 1984. Induced polarization of shaly sands, *Geophysics,* **49**(8), 1267–1287.

Waxman, M.H. & Smits, L.J.M., 1968. Electrical conductivities in oil-bearing shaly sands, *SPE J.,* **8,** 107–122.

Wyllie, R.J. & Southwick, P.F., 1954. An experimental investigation on the S.P. and resistivity phenomena in dirty sands, *Trans. A.I.M.E.,* **201,** 43–56.